Phenomenological Study of Au and Pt nanowires grown in Porous Alumina Scaffolds

By

YONG CHEOL SHIN
B. S., Seoul National University, Korea (2006)
M. S., Seoul National University, Korea (2008)

Submitted to the Department of Materials Science and Engineering
In Partial Fulfillment of the Requirements of the Degree of

MASTER OF SCIENCE
at the
MASSACHUSETTS INSTITUTE OF TECHNOLOGY

February 2011

Author.....
Department of Materials Science and Engineering
December 15, 2010

Certified by.....
Carl V. Thompson
Stavros Salapatas Professor of Materials Science and Engineering
Thesis Supervisor

Accepted by.....
Christopher A. Schuh
Associate Professor of Materials Science and Engineering
Chair, Departmental Committee on Graduate Students

Phenomenological Study of Au and Pt nanowires grown in Porous Alumina Scaffolds

by

Yong Cheol Shin

Submitted to the Department of Materials Science and Engineering on December 15, 2010 in partial fulfillment of the requirements for the degree of Master of Science

Abstract

Porous anodic aluminum oxide, commonly known as AAO, has been widely used as a scaffold to synthesize nanowires and nanotubes. The porous alumina structure can be obtained from a simple electrochemical oxidation process, applying a positive voltage to an aluminum film placed in an electrolyte, and resulting in the formation of periodically arranged arrays of pores. It is possible to tune pore diameters and pore spacing by adjusting parameters such as the type of electrolyte, the pH, and the applied voltage.

Once the barrier oxide is removed from the bottom of the pores, porous alumina that has been formed on conducting substrates can be used for growth of metal nanowires using electrodeposition. We synthesized Au and Pt nanowire arrays on Au or Pt substrates. During electrodeposition, Au nanowires that grew out of the pores developed a pyramid-like faceted shape. This was not observed for overgrown Pt nanowires. To understand this phenomenon, the microstructure and crystallographic characteristics of the overgrown Au and Pt nanowires were studied using SEM, TEM and XRD. It was found that the overgrown Au caps were single crystalline with (111) facets and textured along the [100] direction, while the Au nanowires in the pores were poly-crystalline with a [111] texture. Pt nanowires grown in pores were also polycrystalline and had a [111] texture, but the grain size was much smaller than that of the Au. In contrast with Au, no change of texture or microstructure was observed when Pt grew out of pores. The structure change observed for Au involves nucleation of a new crystal with a (100) texture. This is thought

to be related to the changes in the overpotential that that occur when the Au emerges from the pores.

Thesis Supervisor: Carl V. Thompson
Stavros Salapatas Professor of Materials Science and Engineering

Acknowledgement

This work could be completed with supports from people around me. It should be appreciated through this space.

First of all, I would like to thank Prof. Carl V. Thompson for the guidance for research while I studied at the group. Through his insightful advices, I could approach the problems of my research in the right way.

I am also thankful to my colleagues for all contributions to this research. The cooperation with the CVT group members was so helpful to experiment in the lab. Especially, the discussion with the Wire and Tubes subgroup colleagues, Robert, Shih-wei, Ahmed, Steve, Gilbert, and Jihun was so helpful to figure out the problems and find out the solutions.

It should be noted that the helps of Robert and Sung Keun were so critical for the TEM analysis in this research. Thanks to their dedicated assistance, I could obtain a solid evidence to support hypotheses, which made me complete this thesis.

Finally, I would like to express my gratitude to friends and my family for their supports. Every time I get discouraged, they give me a power to get through the trouble. I hope there will be a day that I can repay their kindness.

The research in this thesis is supported by the MIT Center for Materials Science and Engineering (CMSE).

Table of Contents

List of Figures

List of Tables

Chapter 1. Introduction

1.1 Anodic Aluminum Oxide (AAO) as a Scaffold

1.1.1 Anodization of Aluminum

Anodization of aluminum (Al) is an electrochemical oxidation process in which a positive voltage is applied to Al in an electrolyte, resulting in oxide formation [1-2]. This process has been widely exploited for more than 100 years because it provides an excellent protecting oxide from corrosion and can be produced via a simple procedure [3]. Historically, an ideal model of the porous AAO structure consisting of hexagonally close packed pore arrays was described based on a transmission electron microscopy (TEM) study in 1953 [4]. Between 1970s and 1990s, theoretical efforts to elucidate the growth mechanism of AAO films were actively carried out [5-7]. In 1995, Masuda and Fukuda made the remarkable discovery that certain anodization conditions lead to formation of a self-ordered porous alumina [8]. Since this breakthrough, massive progress on the synthesis of low dimensional nanostructure such as nanowires, nanotubes and nanodots, has been realized in nanotechnology by utilizing porous AAO as a scaffolds with controllable pore diameter and high aspect ratio [9-19].

- Electrochemistry of AAO

  a) Thermodynamics

The formation of alumina from Al in an oxygen ambient or water is a thermodynamically favored reaction involving a large negative Gibb's free energy

change. When Al is electrochemically oxidized, three possible reactions can occur at the anode electrode (the reactions (1)-(3)), whereas hydrogen evolves at the cathode with the reaction of (4).

$$2Al + 3H_2O = Al_2O_3 + 6H^+ + 6e^- \quad , \tag{1}$$

$$Al + 2H_2O = AlO^{2-} + 4H^+ + 3e^- \quad , \tag{2}$$

$$Al = Al^{3+} + 3e^- \quad , \tag{3}$$

and

$$6H^+ + 6e^- = 3H_2 \quad . \tag{4}$$

With an assumption that no complex anion is involved, the equilibrium of each reaction can be determined by the Nernst equation,

$$E = E_0 - \frac{RT}{zF} \ln \frac{[red]}{[ox]} \quad , \tag{5}$$

where R is the universal gas constant, T is the absolute temperature, z is the number of transferred charges, F is the Faraday constant (96,500 C/mol), and brackets indicate concentration of reactants and products of the reaction. For example, the electrode potential E in equation (1) can be given as

$$E = -1.505 - \frac{RT}{3F} \ln[H^+]^3 = -1.505 - 0.059 \, \mathrm{pH} \quad . \tag{6}$$

This equation states that the electrode potential and pH of the electrolyte govern the thermodynamics of the electrochemical reaction. The corresponding diagram describing potential-pH relationship is called a Pourbaix diagram, which for the Al-water system at 25°C is provided in Figure 1.1 [20]. In this system, when a positive voltage is applied to Al in a weakly acidic, neutral or basic solution, oxide formation is favored and governed by the process (1). The resulting compact oxide is called a barrier-type oxide. When the

electrolyte is a strong acid solution with high pH, Al is not oxidized, but dissolves into the aqueous solution instead. This process is called electropolishing [21], with the governing process of (3). When Al is anodized with a mild acid solution such as diluted phosphoric acid, oxalic acid and sulfuric acid, it forms a porous-type oxide. The process can be understood by noting that both Al oxidation (1) and dissolution (3) are involved in the reaction [1]. Since this assumes a slower reaction rate of (3) than (1), the kinetics also should be taken into account.

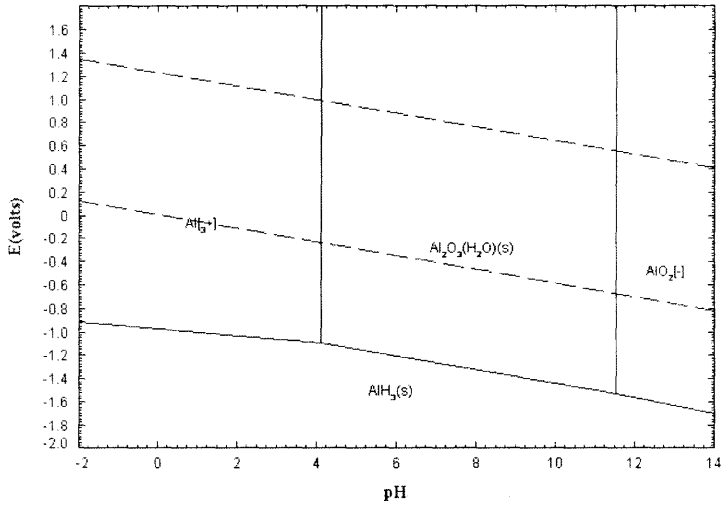

Figure 1.1 The potential-pH diagram, or Pourbaix diagram, of the Al-water system at 25°C [20].

b) Kinetics

There are two interfaces involved in the anodization: the metal (Al)/oxide interface and the oxide/electrolyte interface. First, at the metal/oxide interface, oxygen ions migrate through the oxide due to the high electric field of $10^6 \sim 10^7$ V/cm [1] and

react with Al ions, giving rise to the formation of Al_2O_3,

$$2Al_m + 3O_{ox}^{2-} = Al_2O_3 + 6e^- \quad . \qquad (7)$$

At the oxide/electrolyte, Al ions formed at the metal/oxide interface migrated across the oxide due to the electric field, following two possible reactions depending on the pH of the electrolyte:

with low pH, $$2Al_{ox}^{3+} + 3O_{ox}^{2-} = Al_2O_3 \quad , \qquad (8)$$

with high pH, $$Al_{ox}^{3+} = Al_{aq}^{3+} \quad . \qquad (9)$$

Kinetically, each step can be a rate-limiting step, as shown in Table 1.1 [22]. Since the current passing across the oxide film is predominantly ionic, the kinetics of Al anodization follows the Guntherschultze-Betz equation,

$$j_i = j_0 \exp(\beta E) \quad , \qquad (10)$$

where j_i is the ionic current density with both anionic and cationic contributions, j_0, β are material- and temperature-dependent parameters, respectively, and E is the electric field across the oxide [23].

- Pore formation mechanism

Various models for pore formation mechanism have been proposed [24-29]. The detailed description of each model is out of scope of this thesis; therefore in this section, the field-assisted dissolution model and a strain-induced instability model recently proposed by J. Oh [30] is briefly introduced.

Authors	Ref.	Ion	Rate determining step	Field strength	Kinetics
Güntherschulze and Betz (1934)	109	+, −	ox	$E=\Delta U/d$	$i=i_0 \exp(\beta E)$
Verwey (1935)	110	+	ox		$i=i_0 \exp(\beta E)$
Mott and Cabrera (1947)	113	+	me/ox	$E=$ const.	$i=i_0 \exp(\beta E)$ $1/d=a-b \ln(t)$
Vermilyea and Vetter (1955)	176	+	ox	$E=\Delta U/d$	$i=i_0 \exp(\beta E)$ $dd/dt=Ai_0 \exp(\beta E)$
Cohen and Sato (1964)	114				$d=A+B \ln(t+t_0)$ Collective place exchange
Fehlner and Sato (1964)	179	−	ox/el	$E=$ const.	$d=A+B \ln(t+t_0)$ $W=f(d)$
Macdonald *et al.* (1981, 1991)	107	+, − e^-, h^+	ox me/ox ox/el	$E=$ const. No $f(d,U)$	Point defect model

Table 1.1 Kinetic models for oxide growth by anodization [22].

a) Field-assisted dissolution model

The growth of porous-type AAO can be described as a dynamic equilibrium between the oxide formation at the metal/oxide interface and oxide dissolution at the oxide/electrolyte interface. However, it is known that the purely chemical dissolution rate of the oxide is very low compared to the oxide formation rate. To account for the equilibrium, local joule heating at the pore bottom was considered as what enhances the dissolution rate, but the actual temperature increase during the process is not significant. Alternatively, it can be assumed that the electric field at the pore bottom is locally concentrated due to the geometry and greatly promotes the dissolution of the oxide at the oxide/electrolyte interface, giving rise to the establishment of the dynamic equilibrium [24]. The work by O'Sullivan and Wood [5] provided a basis supporting this mechanism theoretically. They supposed that the rate-limiting step of the dissolution is the bond-breaking step between Al and O at the oxide/electrolyte interface. As shown in Figure 1.2,

the Al-O bonds can be affected by hydrogen bonding in aqueous electrolyte, but not significantly. The application of an electric field, however, stretches the bond along the field direction, thereby lowering the activation energy for the dissolution. Consequently, the oxide dissolution rate can significantly increase, competing with the oxide formation rate. Since the electric field is concentrated at the pore bottom, the reaction proceeds vertically, and thus a cylindrical pore array forms.

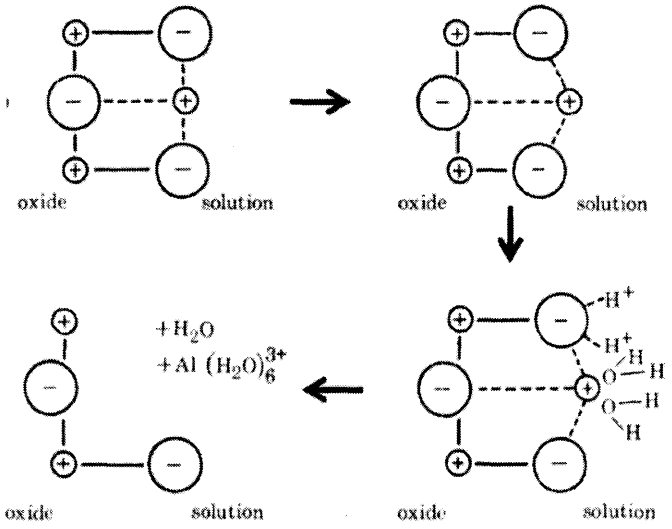

Figure 1.2 Schematic field-assisted dissolution process [5].

b) Strain-induced instability model by J. Oh [30]

Although the field-assisted dissolution provided a key to elucidate pore formation mechanisms in the anodization process, it was not found that experimental results fit to a model based on this mechanism [31]. J. Oh attributed the discrepancy to the failure of the

determination of the field-assisted dissolution rate on a planar surface. He separated the kinetic and morphological interaction between the metal/oxide interface and the oxide/electrolyte interface by discontinuously anodizing Al. After the pre-formation of the barrier-type AAO on Al, the anodization process to form a porous-type AAO was followed without further oxidation at the metal/oxide interface. As a consequence, it was observed that two types of pores developed, depending on driving instabilities. The first pore formation was based on the field-assisted dissolution mechanism. When the applied electric field exceeded a critical value, incipient pores started to form. The resulting spacing of the pores was, however, much smaller than what was expected from the given anodization condition, implying that the field-assisted dissolution model does not account for the conventional anodization process. When the electric field was further increased, the development of secondary pores driven by another instability was initiated and led to larger pore spacing. This was attributed to the mechanical stress increase caused by the insertion and transport of ions as well as the volumetric expansion during the oxidation. In other words, there is a critical stress that can give rise to the formation of larger pores. In addition, it was also believed that the pore growth in the steady state was achieved by the balance of the oxide formation flux at the metal/oxide interface with the flux of the plastic flow of the oxide toward the pore walls, leading to a self-ordered hexagonal pore array.

- Self-ordered porous AAO

After Masuda and Fukuda discovered the anodization condition that leads to ideally close packed hexagonal pore arrays [8], other stable anodization conditions have

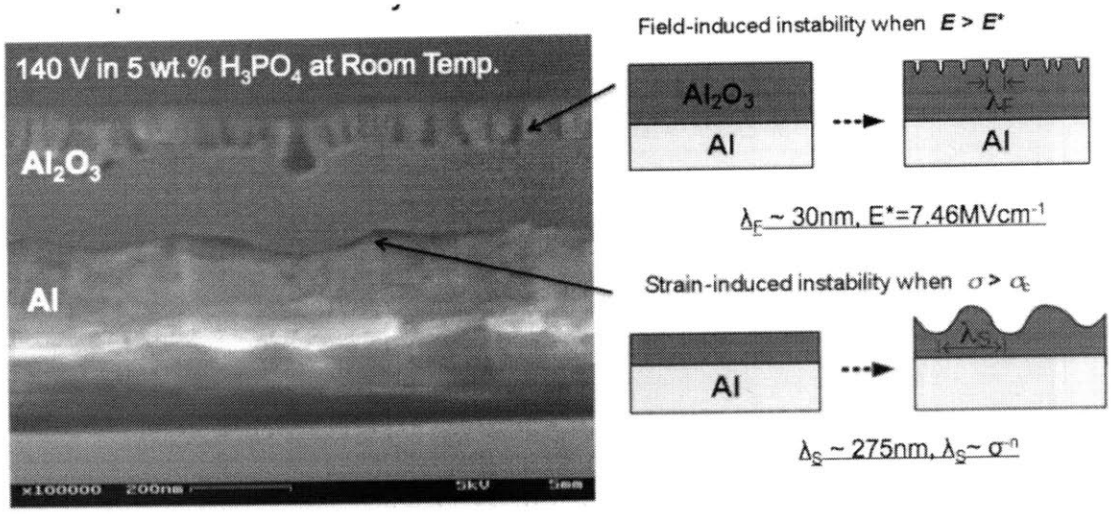

Figure 1.3 Independently developed pore structure with respect to the different instability origins. The formation of the large pores associated with conventional anodization process was attributed to a strain-induced instability [30].

been sought. The method of Masuda and Fukuda using 0.3 M oxalic acid at 0°C with application of a constant voltage of 40 V can lead to an ordered pore array with 100 nm pore spacing. Further anodization conditions with 50, 65, 100, 420, and 500 nm pore spacing were 19 V and 25 V in sulfuric acid, 40 V in oxalic acid, and 160 V, 195 V in phosphoric acid, respectively [32-35]. These conditions are called mild anodization. In contrast, other anodization conditions with a fast growth rate were discovered, which are called hard anodization. Lee et al. fabricated self-ordered pore arrays with 220-300 nm of pore spacing by hard anodization condition with the constant voltage of 120-150 V applied in 0.3 M oxalic acid at 1°C [36]. Various anodization conditions leading to the formation of a self-ordered pore arrays are illustrated in Figure 1.4 [36]. In this thesis, as a mild and a hard anodization condition, 86 V at 25°C in 5 wt. % phosphoric acid and 19 V at 3°C in 0.3 M sulfuric acid were used, respectively.

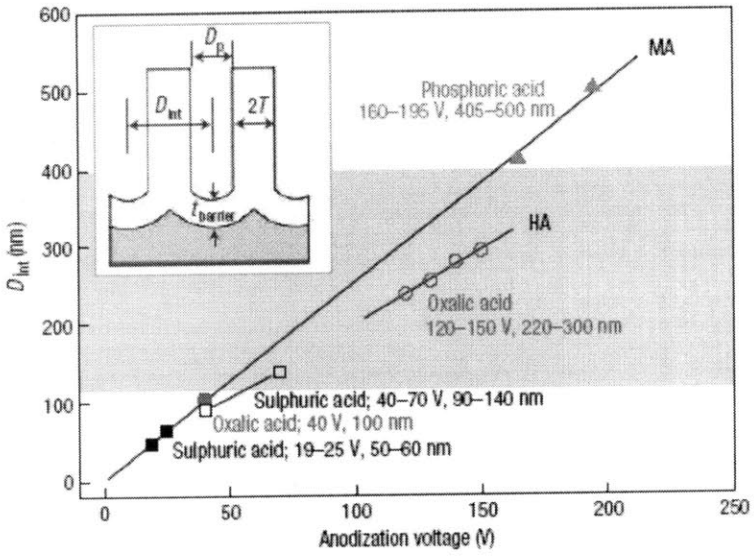

Figure 1.4 Various mild and hard anodization conditions to synthesize self-ordered pore arrays with specific pore spacing [36].

1.1.2 Selective Barrier-oxide Perforation

As stated previously, porous AAO is one of the prominent template materials used to synthesize highly ordered nanowire or nanotube arrays with pore diameters as low as a few tens of nanometers and with a lengths of tens of micrometers. The specification of nanostructure is determined by the anodization conditions. When the nanostructure is integrated in the AAO scaffolds by electrochemical methods, such as electrodeposition, the exposure of an electrically conductive underlayer to the electrolyte through the pores is desired. In terms of processing, however, there are two important requirements the AAO scaffolds/underlayer structure should have. First, the barrier-oxide in the pore bottom should be selectively etched without a modification of pore structure such as pore widening and the delamination of pores array from the underalyer. Moreover, the

electrochemical reactivity of the underlayer should not affect to the AAO formation during anodization. J. Oh suggested tungsten (W) as an underlayer [18]. When he anodized an Al/W bi-layer, it was discovered that locally formed WO_3 perforated the pore bottoms by volumetric expansion as illustrated in Figure 1.5. Then, since only WO_3 is dissolved in an aqueous solution with pH 7, it could be selectively etched in a pH 7 buffer solution. As a result, a highly ordered nickel (Ni) nanowire array could be synthesized via electrodeposition [18].

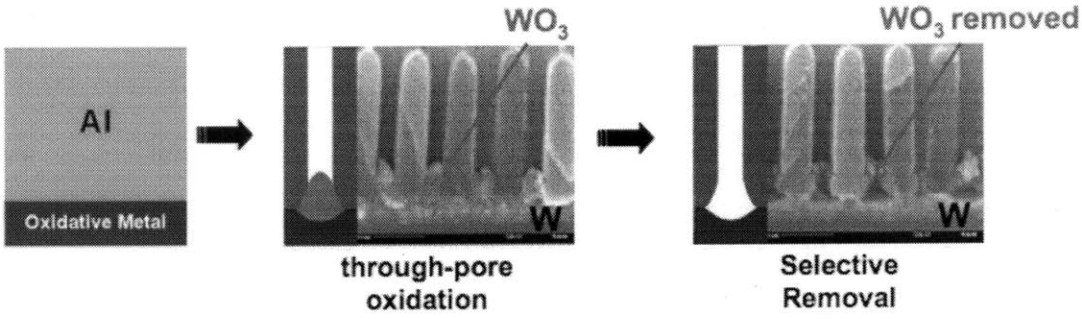

Figure 1.5 Schematic and SEM images of the selective barrier oxide perforation process [18].

Furthermore, beyond the Al/W bi-layer structure defining the underlayer, an Al/W/substrate tri-layer structure was used to provide freedom to choose other substrate materials to act as an electrode during electrodeposition [30]. In this structure, what was challenging was optimization of the thickness of the W interlayer for each anodization condition. When the W interlayer is thin, thereby resulting in thin WO_3, the electric field across the WO_3 will be strong enough to drive excessive oxygen ions to the substrate. It can induce a sharp increase of anodic current during the anodization by O_2 evolution at the substrate surface. On the other hand, with a thick W thickness, the complete

consumption of W after Al/W anodization might not be possible because the W oxidation process is self-limiting. Consequently, W can be still present on the substrate material after the WO_3 etching. The exact W interlayer thickness with respect to anodization condition was determined by measuring the depth of dimples on the W interlayer surface originating from W consumption to form the perforating WO_3 at the pore bottoms, which is shown in Figure 1.6. The tri-layer structure with the optimum W thickness can be utilized to fabricate 1-D nanostructure on any substrate required for various applications.

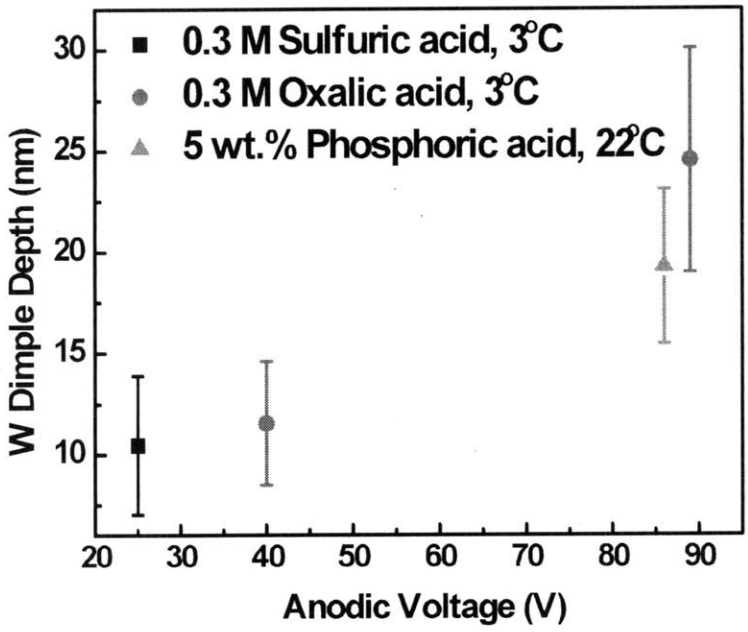

Figure 1.6 The dimple depth of a W interlayer with respect to the anodization conditions for an Al/W/substrate tri-layer structure. This indicates the volume of W consumed to form WO_3 during Al/W anodization and determines the optimum W interlayer thickness [30].

1.2 Crystallography of Metal Nanowires

1.2.1 Growth Mechanism of Elctrodeposited Nanowires

Electrodeposition is a complicated process that involves charge transfer, diffusion, chemical reactions, chemical adsorption and different properties of different substrates. Moreover, for the metal nanowires grown on the AAO scaffolds via electrodeposion, the confinement caused by pore walls should be also taken into account. As schematically shown in Figure 1.7 [37], there are three basic mechanisms for formation of a deposit, depending on the binding energy of metallic atoms on the foreign substrate (Υ_{ms}) compared with corresponding metallic atoms on the same material (Υ_{mm}), and on the crystallographic misfit characterized by lattice constant d_m and d_s of the metal and substrate in the bulk phase. The Volmer-Weber growth model (Fig. 1.7(a)) indicates that 3D metal islands form by nucleation and coalescence to form a film for $\Upsilon_{ms} << \Upsilon_{ms}$. On the other hand, Fig. 1.7(b) and (c) represent 2D layer growth modes: the Frank van der Merwe growth mode, (b), with $\Upsilon_{ms} >> \Upsilon_{ms}$ and the misfit $(d_m-d_s)/d_s \approx 0$ and the Stranski-Krastanov growth mode, (c), with $\Upsilon_{ms} >> \Upsilon_{ms}$ and the misfit $(d_m-d_s)/d_s > 0$.

For a 3D-like nucleus such as shown in Fig. 1.7(a), the critical nucleus size (N_c) that can grow further is given as [37],

$$N_c = \frac{8BV_m^2\sigma^3}{27(ze|\eta|)^3} \quad , \tag{11}$$

where V_m, σ, z and B are the atomic volume of the metal, the surface energy, the effective electron number and a constant, respectively, and η is the overpotential defined as,

$$\eta = E(I) - E_0 , \tag{12}$$

where E(I) and E_0 are the external current induced potential and the equilibrium potential of the electrode, i.e. the open circuit potential, respectively. For a 2D-like nucleus such as

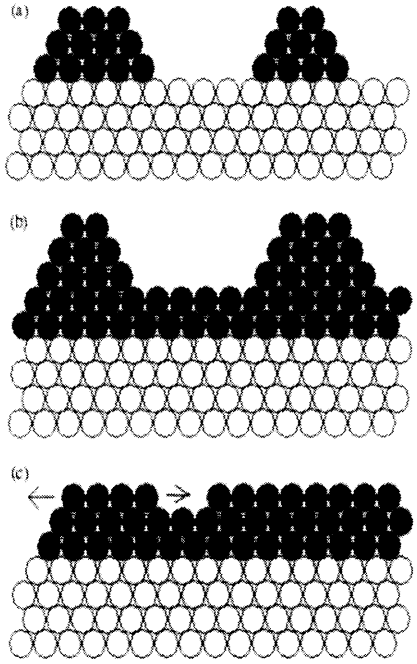

Figure 1.7 Schematic illustration of different growth modes in metal deposition on foreign crystalline substrates [37].

shown in Fig. 1.7(b), N_c is expressed as [37],

$$N_c = \frac{bs\varepsilon^2}{(ze\eta)^2} \quad , \tag{13}$$

where s, ϵ, z and b denote the atomic area, the edge energy, the effective electron number and a constant, respectively.

1.2.2 Metal Nanowires grown on AAO Scaffolds

Metal nanowires grown in AAO scaffolds can be either poly-crystalline or a single crystal with a growth on preferred crystallographic planes, depending on the elctrodeposition conditions employed [38-45]. Tian et al. attributed the single crystal structure of the electrodeposited low-melting-point metallic nanowires, such as Au, Ag

and Cu, to the formation of a 2D-like nucleus under lower overpotential, because the smaller the overpotential, the larger N_c, and the more favorable is the formation of single crystal nanowires, as expected from Eq. (13) [38]. Relative to the low melting point metallic nanowires, high melting point metals such as Co, Ni and Pt, have smaller atomic volumes and higher effective electron numbers, resulting in a smaller N_c. In addition, the diffusion of electrodeposited atoms along the surface is constrained by the high cohesive energy of the metals, thereby causing the nucleation and coalescence of 3D grains. Therefore, instead of forming a single crystal structure, a polycrystalline structure with a small grain size is usually observed. In general, the texture of single crystal face centered cubic (FCC) metal nanowires are the either (111) or (220). The crystallographic texture can be defined by that of the first 2D nucleus. The lower the surface free energy, the lower is the energy needed and, consequently, the overpotential to obtain such an orientation is reduced. In other words, the texture thermodynamically follows the tendency of minimization of surface energy during electrodeposition. In terms of processing, however, other parameters such as the applied overpotential, temperature and pH involved in electrodeposition, affect the growth kinetics. Under low overpotential closer to the equilibrium condition, preferred texture along the [111] direction is expected in FCC metal nanowires, since this is the lowest surface energy plane. On the other hand, it is generally known that the higher overpotential leads to (220) texture [46-47]. Switzer et al reported that cuprous oxide (Cu_2O) thin films grown by electrodeposition on an Au (100) substrate showed a change of preferred texture from [100] to [110] when a higher overpotential than a critical value was applied [46]. This was interpreted to mean that at high overpotential, where the system is far from equilibrium, the kinetically favored

texture along [110] developed through a new nucleation event. This can be accounted for the promoted adsorption of hydrogen ions on the cathode, driven by the increase of the overpotential, which stabilizes the (110) plane [47].

For these reasons, a higher overpotential kinetically favors a preferred texture along the [110] direction in single crystalline FCC metal nanowires, and the stabilization of the (110) plane by hydrogen adsorption prevents the formation of nanowires with [111] orientations. With an intermediate overportential, polycrystalline structures form due to the competition between [111] and [110] directions.

1.3 Thesis Overview

In chapter 2, we report an experimental process in detail, ranging from the preparation of substrates, the fabrication of AAO scaffolds and synthesis of nanowires to their characterization using X-ray diffraction (XRD) and TEM.

In chapter 3, we report the experimental results. In the fabrication part, preparation of AAO scaffolds with different structures using tri-layer substrates is discussed. Then, description of the synthesis of freestanding Au and Pt nanorwire arrays via electrodeposition follows. Interestingly, we find that overgrown Au nanowires are faceted but Pt nanowires are not. In the characterization part of chapter 3, we confirm the strong (100) texture in the overgrown Au nanowires and show that the overgrown parts, 'caps', are single crystals along with [100]. In contrast, a weak texture of the Pt nanowires is observed.

In chapter 4, we describe a mechanism that can account for the observed behavior of the Au and Pt nanowires. The difference between Au and Pt is attributed to the

different nucleation models outlined above for electrodepoistion; while the Au nanowire forms from a 2D-like nucleus, Pt nanowires are nucleated as 3D structures. We understand the formation of single crystal Au nanowires as originating from the dynamic change in overpotential during the electrodeposition.

Finally, chapter 5 summarizes the findings and discussion in the previous chapters. This chapter also suggests future research.

Chapter 2. Experimental Technique

2.1 Overview

The experiments consisted of four processes: substrate preparation, anodization, electrodeposition, and characterization. Four different substrates were prepared to observe the effect of the electrode material (Au or Pt) and the diameter of the nanowires depending on the specific anodization conditions required. Through the electrodeposition process, both freestanding Au and Pt nanowires were synthesized. All the fabrication processes were analyzed with scanning electron microscopy (SEM). To study the microstructure and crystallographic properties of the nanowires, X-ray diffraction (XRD) and transmission electron microscopy (TEM) were used.

2.2 Sample Fabrication

2.2.1 Substrates

Three tri-layer substrates with different stacks were prepared. All the metal thin films were deposited on thermally oxidized as-received 6-inch silicon 100 wafers via multi-source electron beam evaporation (Temescal Model VES2550) in a high vacuum (HV) system. The base pressure was 1.5×10^{-6} Torr and the thickness of each metal layer was determined with a quartz crystal monitor. The specific stack structures and thicknesses are given in Table 2.1. To prevent the deposited thin film stacks on silicon oxide from delaminating, a titanium (Ti) thin film as an adhesion layer was deposited on the silicon oxide.

	Stack (nm)
substrate A	Al(500)/W(15)/Au(200)/Ti(20)
substrate B	Al(450)/W(15)/Pt(200)/Ti(15)
substrate C	Al(450)/W(7.5)/Au(200)/Ti(15)
substrate D	Au(200)/Ti(15)

Table 2.1. The stack structure of the prepared substrates.

2.2.2 Anodization

- Anodization

The experimental setup for anodization is depicted in Figure 2.1 [23]. The substrates were anodized with a potentiostat/galvanostat system (Keithley Model 2400) as shown in H of Fig. 2.1. The cell consists of two electrodes: an Al thin film layer on the top of the substrates as a working electrode and a Pt mesh soaked in electrolyte as a counter electrode (F and B in Fig. 2.1, respectively). The diameter of the working electrode exposed to the electrolyte was 0.9 cm. All the processes were controlled by a computer connected to the potentiostat/galvanostat via a GPIB cable (I in Fig. 2.1). A motor-controlled rotator (A in Fig. 2.1) stirred the electrolyte during the anodization process.

Two anodizaiton conditions were used. While substrates A and B were anodized with a 5 wt.% phosphoric acid (H_3PO_4) solution at room temperature by applying a constant voltage of 86V, substrate C was anodized with a 0.3 M sulfuric acid (H_2SO_4) solution at 3°C by applying a constant voltage of 19 V. To perforate the pore bottoms with WO_3, the anodization continued without changing a process parameter for more or less 150 seconds (s) after the Al was completely oxidized. The process was confirmed by

monitoring a time vs. anodic current curve. Finally, the resulting sample was rinsed with deionization (DI) water.

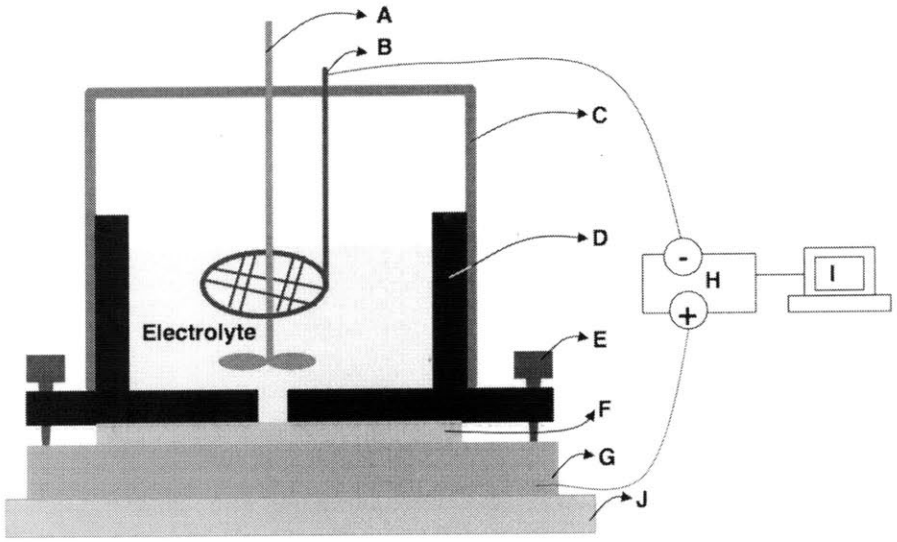

Figure 2.1 A schematic diagram of the apparatus for anodization. A: motor-controlled rotator, B: Pt mesh as a counter electrode, C: styrofoam isolator, D: teflon electrolyte container, E: screw to fix the container to a brass plate, F: prepared substrates with Al thin film layer on top, G: brass plate connected to the anode, H: potentiostat/galvanostat, I: computer to control the potentiostat/galvanostat via GPIB, and J: Peltier cooling element [23].

- WO_3 etching

To expose a working electrode layer (Au for substrate A and C, and Pt for substrate B) in the electrodeposition process, WO_3 was removed using a pH 7 buffer solution (a mixture of sodium phosphate and potassium phosphate with pH 7 at 25°C, VWR International). The etching was implemented for 15 minutes at room temperature with agitation and then the sample was rinsed with DI water.

2.2.3 Electrodeposition

- Au electrodeposition

Au nananowires were grown on substrates A, B and C with AAO scaffolds via electrodeposition using a commercial Au electroplating solution consisting of 5-10% sodium gold sulfate and 1-5% of additives (BDT®510, Ethone) at room temperature. For comparison with nanowire structures, a Au film was also electrodeposited on the substrate D without AAO scaffolds. A two-electrode system was employed as in the anodization process, but there were two differences in the process parameters. First, a constant current density of 1.0 mA/cm^2 was maintained during the process while a constant voltage was applied in the anodization process. Second, in contrast with the anodization process, a Pt mesh counter electrode was connected to the anode to induce a reduction reaction of Au ions at the working electrode. The motor-controlled rotator stirred electrolyte during the electrodeposition process as well. The process was monitored by recording the cathodic voltage as a function of time. When the process finished, the sample was separated from the electrochemical cell and then rinsed with DI water.

- Pt electrodeposition

Pt nananowires were grown via a three-electrode potentiostat/galvanostat system (PGSTAT 100, AUTOLAB) using a solution of 5 mM K_2PtCl_4 (Alfa Aesar) in 1.2 mM hydrochloric acid (HCl) at room temperature with application of the constant voltage of 0.01 V with respect to a Ag/AgCl reference electrode (Beckman). For Pt nanowire synthesis, only substrates A and C were used. The process was monitored by measuring

the current curve over time. When the process finished, the sample was also separated from the electrochemical cell and then rinsed with DI water.

- AAO etching

Finally, to obtain freely standing nanowire arrays, the AAO scaffolds were removed by wet etching. The process was carried out using an etchant of 25 wt.% of tetramethylammonium hydroxide (TMAH, SACHEM, INC) solution at 60°C for 2 hours. During this process, the W layer under the pore wall was also completely etched. When the process finished, the samples with only freestanding nanowires on the substrates were rinsed with isopropanol and DI water in sequence.

Figure 2.2 schematically illustrates the experimental processes for synthesizing freestanding nanowire arrays. Although the figure shows the process for Au nanowire fabrication on a Au substrate, processes for other materials followed the same procedures.

2.3 Characterization

2.3.1 Scanning Electron Microscopy (SEM)

Every fabrication step was confirmed using an SEM (5 kV of acceleration voltage, Zeiss Gemini 986). The images were taken by mounting samples on a stub tilted at 70° or plane. For a charging issue, the images of AAO were obtained after sputtering 0.5 nm of Au on the sample. For energy-dispersive X-ray spectroscopy (EDX) analysis, a field-emission high-resolution SEM (5.4 kV acceleration voltage, JEOL 6320 FV) was also used.

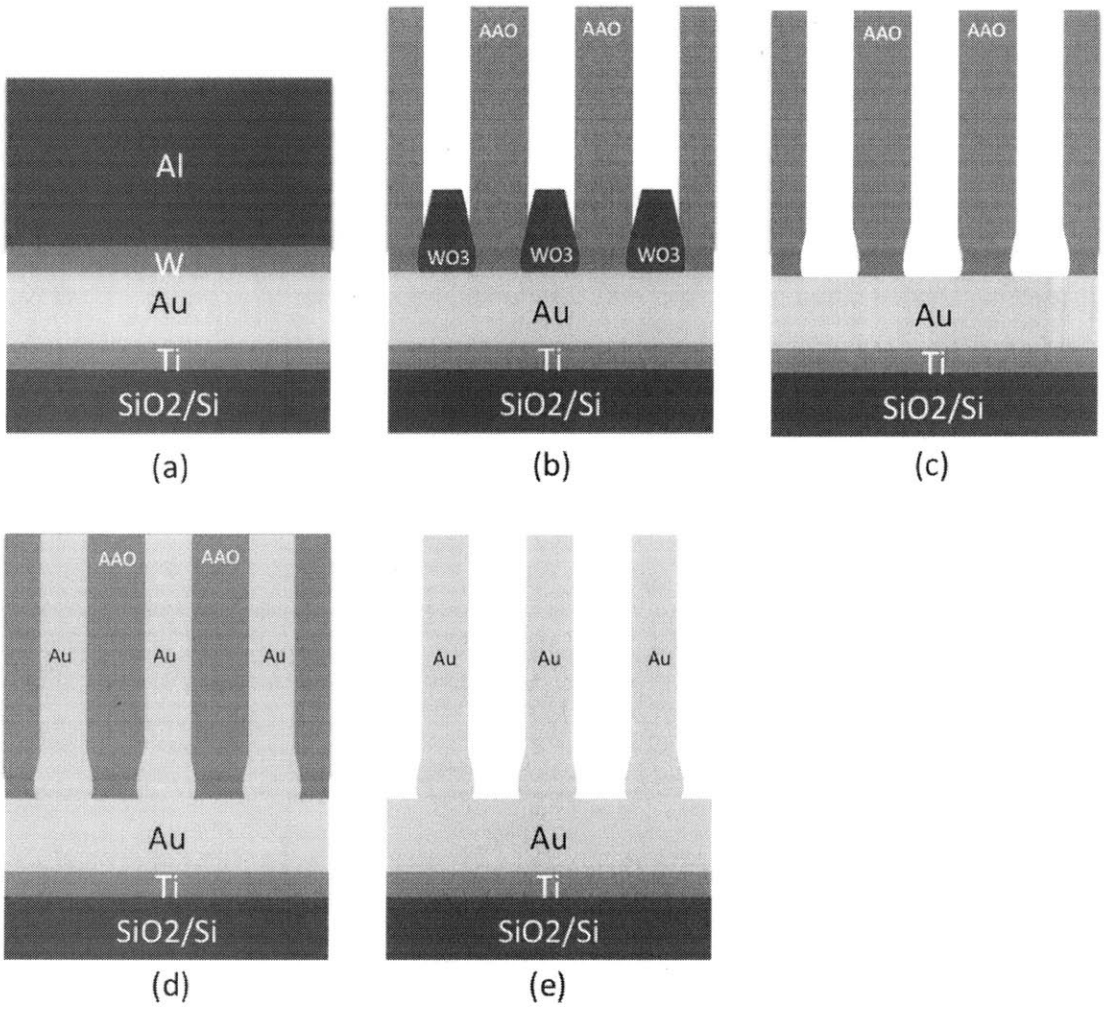

Figure 2.2 Schematic process flows for nanowire fabrication. (a) as-prepared substrate, (b) anodization, (c) etching of WO_3 using a pH 7 buffer solution, (d) Au electrodeposition, and (e) etching of AAO scaffolds and W layer using a TMAH solution at elevated temperature, leaving freestanding nanowires array on the substrate.

2.3.2 X-ray Diffraction (XRD)

The crystallographic texture of the nanowires was studied using X-ray diffraction (XRD, PANlytical X'Pert Pro). The acceleration voltage and current were 45 kV and 40 mA, respectively. XRD results were obtained from Cu Kα radiation in the theta-2theta

mode. To avoid strong signal intensity in the diffraction peaks from the silicon substrate, 1° of offset was applied to the value of 2theta, which did not affect the position and intensity of other diffraction peaks.

2.3.3 Transmission Electron Microscopy (TEM)

While the crystallographic texture of the collective nanowires was characterized via XRD analysis, that of individual nanowires was studied using a TEM (JEOL 2010 and JEOL 2010F). The microstructure of a nanowire, which could not be imaged using the SEM, was also analyzed using the TEM. In addition, the crystallinity of a nanowire was confirmed by a selective area electron diffraction (SAED) pattern. To prepare the sample for TEM imaging, the freestanding nanowires were soaked in isopropanol and then sonicated for an hour to separate them from the substrate. With a plastic pipette, drops of isopropanol solution with floating nanowires were dispensed onto a TEM grid and dried for at least three hours.

Chapter 3. Results

3.1 Overview

Au and Pt nanowires were fabricated via electrodeposition with AAO scaffolds. With excessive electrodeposition time, the Au and Pt nanowires grew three-dimensionally out of the pores. It was found that the overgrown Au was faceted whereas the overgrown Pt did not show this behavior. To understand this phenomenon, crystallographic texture and microstructure analysis using XRD and TEM was used. The XRD results suggested that the overgrown Au 'cap's led to a strong texture change to the [100], but Pt did not, Moreover, a much larger crystallite size was also estimated, implying that the overgrown Au might be single-crystalline, as suggested from the faceted shape. The TEM results for the Au nanowires confirmed the presumption that the overgrown Au caps were (111) faceted single crystal structure with a preferred texture along [100].

3.2 Nanowire Fabrication

3.2.1 AAO scaffolds

As stated in 2.2.2, two anodization conditions were employed to the prepared substrates. While substrates A and B were anodized with a 5 wt. % of phosphoric acid solution by applying a constant voltage of 86 V at room temperature (mild anodization), substrate C was anodized with a 0.3 M sulfuric acid solution by applying a constant voltage of 19 V at 3°C (hard anodization). After the anodization, WO_3 was selectively

removed by wet etching with a pH 7 buffer solution for 15 minutes at room temperature.

In Figure 3.1, an anodic current vs. time curve under a mild anodization in the case of substrate A is shown. As seen in the curve, the anodic current gradually increases in the steady state, indicating that the AAO scaffolds have formed. After about 10 minutes there was a sudden current drop when the oxidation of Al was completed and WO_3 started to form at the pore bottom. It can be presumed that locally concentrated electric field enhances the oxidation of W, so that WO_3 penetrates the pore bottom due to a volumetric expansion. In contrast with the formation of the AAO, since the WO_3

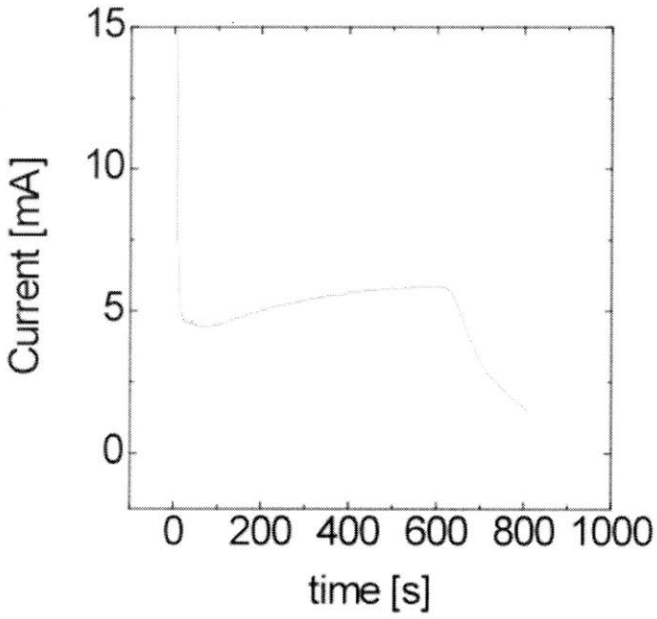

Figure 3.1 An anodic current vs. time curve under a mild anodization condition with substrate A. The Al oxidation and the W oxidation step are clearly distinguishable. The anodic current increased during the formation of porous aluminum oxide. When the Al was completely oxidized, the current started to decrease as W started to oxidize, since the W oxidation process is self-limiting.

formed with phosphoric acid or sulfuric acid is a barrier-type oxide and the process is self-limiting, the growth rate of the WO_3 gradually decreases as the WO_3 thickens. This behavior was confirmed through the decrease of anodic current after W starts to oxidize around 800s in Fig. 3.1. An anodic current vs. time curve like the one shown in Fig. 3.1 was observed in both the mild and hard anodization. The current drop occurred at about 600s, indicating that the oxidation rate of Al was 1.2 nm/s.

Before electrodeposition to fabricate nanowires, it was essential to verify the WO_3 was completely removed and the bottom electrode layer was exposed. Figure 3.2(a) and (b) show SEM images of the AAO scaffolds before WO_3 etching, i.e. as-anodized and after etching with a pH 7 buffer solution. The mild anodization condition above was applied on a templated substrate A prepared via interference lithograph (IL). As shown in the figure, it was observed that WO_3 was selectively etched through the process (orange

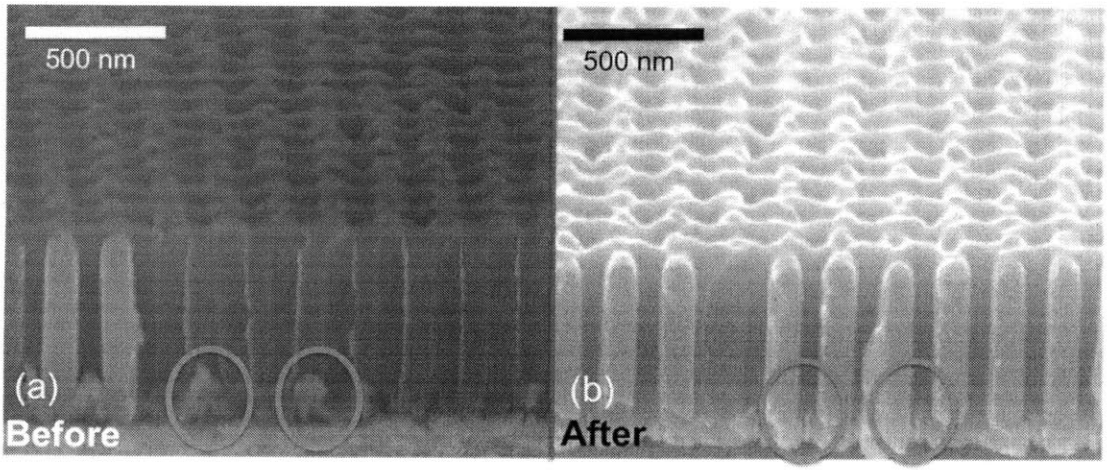

Figure 3.2 SEM images of the AAO scaffolds (a) before and (b) after WO_3 etching by soaking in a pH 7 buffer solution for 15 minutes at room temperature. It was observed that WO_3 was selectively removed through the process (orange circles).

circles) without a structural modification of the AAO scaffolds.

Although the etching of WO_3 is clearly observable through the SEM images in Fig. 3.2, an energy-dispersive x-ray spectroscopy (EDX) analysis was also implemented to quantitatively confirm that WO_3 was selectively removed and the bottom layer was exposed. The same mild anodization and WO_3 etching conditions applied to the Al/W/Au tri-layer in Fig. 3.2 were applied to an untemplated substrate A. For the EDX analysis, the scaffolds were selectively removed by exfoliating with an adhesive tape, thereby leaving only the W layer without scaffolds on the Au layer. Schematically, it can be described as the structure in Fig. 2.2(c) where only the AAOs are removed. After imaging a plan-view of the structure, the EDX was conducted at the positions corresponding to the W/Au bi-layer and Au layer. The SEM images and EDX results are shown in Figure 3.3. As can be

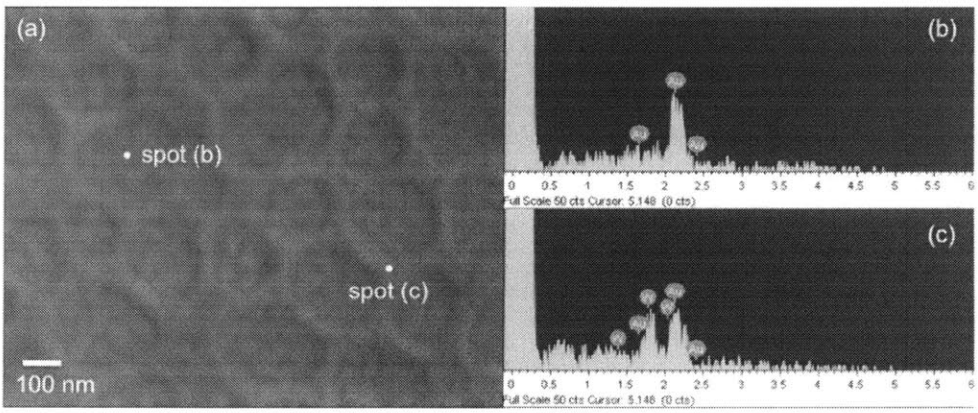

Figure 3.3 (a) SEM image of the W layer on the Au substrate after exfoliating the AAO scaffolds using an adhesive tape. (b) and (c) are the EDX results corresponding to the positions in (a) of the Au layer and W/Au bi-layer, respectively. The result (b) verified that WO_3 formed during the anodization process was completely and selectively removed by the etching process with a pH 7 buffer solution.

seen in the SEM image, EDX is obviously able to distinguish the W layer from the Au substrate. As expected in 1.1.2, the EDX results confirmed the observation again that WO_3 was completely removed by the etching process because only Au was detected in the spot (b) in Fig. 3.3(a) where the WO_3 formed during the anodization process. Quantitatively, 100 at. % of Au was found on the spot (b) whereas 39 at. % of W and 61 at. % of Au were detected on the spot (c).

AAO scaffolds fabricated with different anodization conditions are shown in Figure 3.4. These images were taken after WO_3 was removed. As can be seen in Fig. 3.4(a) and (c), the AAO scaffolds with 80 nm pore diameter and 200 nm pore spacing were obtained under the mild anodization process. On the other hand, the AAO scaffolds with 15 nm pore diameter and 50 nm pore spacing were fabricated through the hard anodization process, as shown in Fig. 3.4(b) and (d).

3.2.2 Nanowires fabrication

- Au nanowires

Figure 3.5 shows a cathodic voltage vs. time curve obtained from an electrodeposition process to fabricate Au nanowires on the Au layer as a working electrode. A constant current density of 1.0 mA/cm^2 was maintained during the process. The curve could be divided into three parts. The first increase of voltage (0-40s) indicated the nucleation of Au on the substrate. The next voltage increase step (40-100s) corresponded to the vertical growth of Au in pores, forming nanowires. Due to the confinement effect with respect to the pore walls, electric resistance gradually increased to maintain a constant current, i.e. the growth rate. When Au electrodeposition proceeded

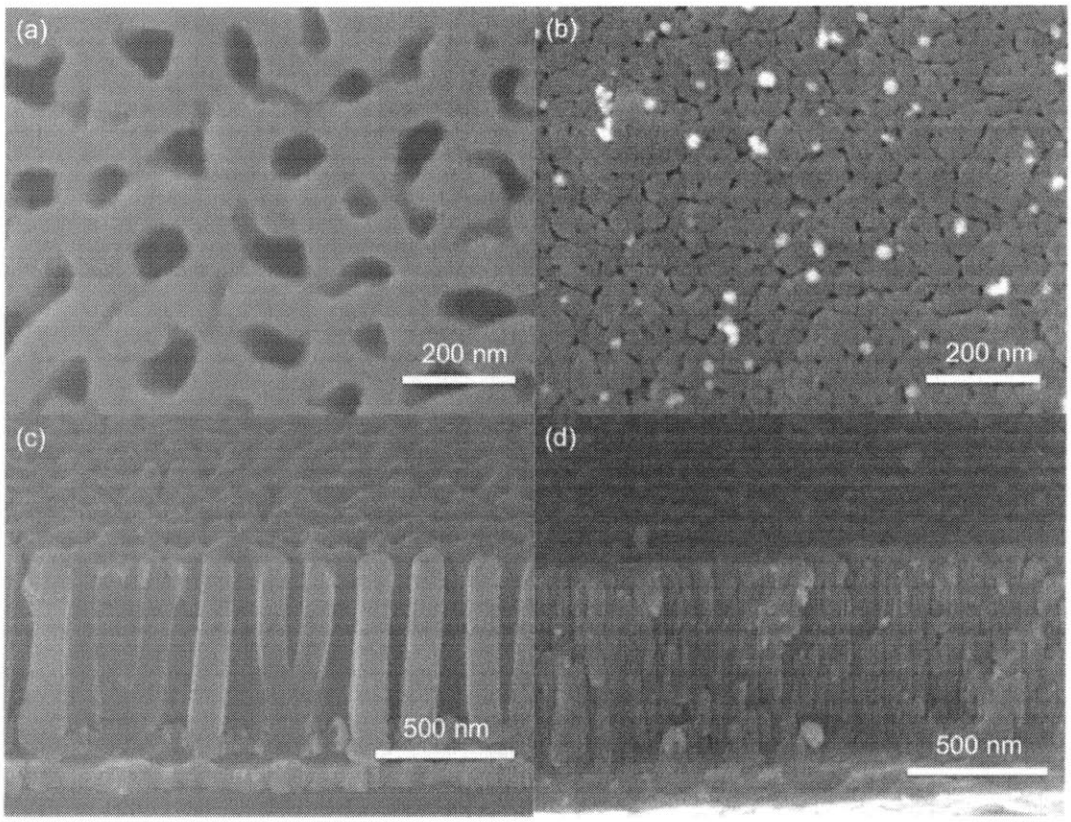

Figure 3.4 SEM images of the AAO scaffolds fabricated via different anodization conditions. (a) and (c) are plan-view and cross-sectional views of the AAO fabricated with the substrate A under mild anodization. The resulting AAO scaffolds showed 80 nm pore diameters and 200 nm pore spacing. (b) and (d) are plan-view and cross-sectional views of the AAO fabricated with the substrate C under the hard anodization conditions. The resulting AAO scaffolds have 15 nm pore diameters and 50 nm pore spacing.

longer than 100s, the cathodic voltage started to drop and finally was saturated. This was interpreted to mean that the electrodeposition in pores complete at around 100s and additional processes gave rise to a three-dimensional growth of Au out of pores. Since the confinement effects the growth of Au, the voltage to maintain a constant current density was lowered and saturated in the steady state. This behavior was also observed in the Au electrodeposition on the substrate B and C. Therefore, the process should be stopped at an

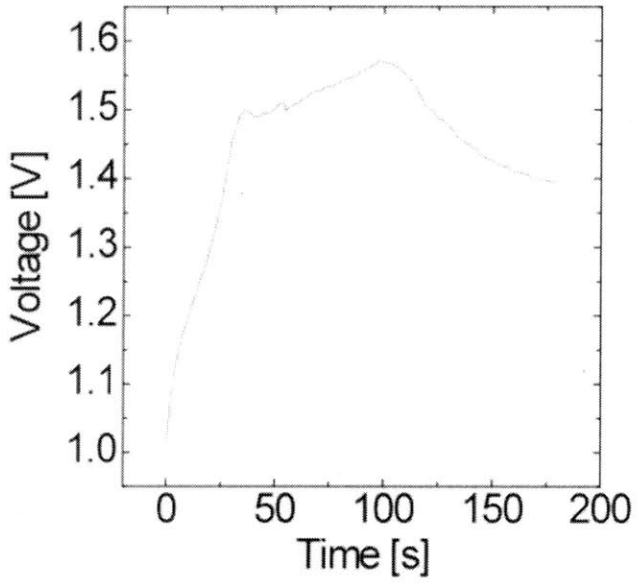

Figure 3.5 A cathodic voltage vs. time curve from a Au electrodeposition process on the substrate A. The process can be divided into three parts; nucleation of Au (0-40s), growth in pores (40-100s), and three-dimensional growth out of pores (after 100s). Other Au electrodeposition processes on substrates B and C showed a similar trend.

appropriate moment to obtain nanowire arrays without overgrowth, by monitoring the voltage vs. time curve because it is not a self-limiting process. Although a nucleation step was involved, the estimated growth rate of Au nanowires was roughly 7 nm/s, calculated from the 700 nm AAO thickness divided by 100s until the cathodic voltage began to drop.

Figure 3.6 shows SEM images of the Au nanowire arrays grown on the substrate A with respect to the deposition time. Corresponding electrodeposition times for (a), (b), (c), and (d) were 70s, 90s, 110s, and 180s, respectively. To observe the relative difference of nanowire length, the images were taken with the AAO scaffolds. As can be seen in (c) and (d), vertically growing Au nanowires in pores ((a) and (b)) started to expand three-

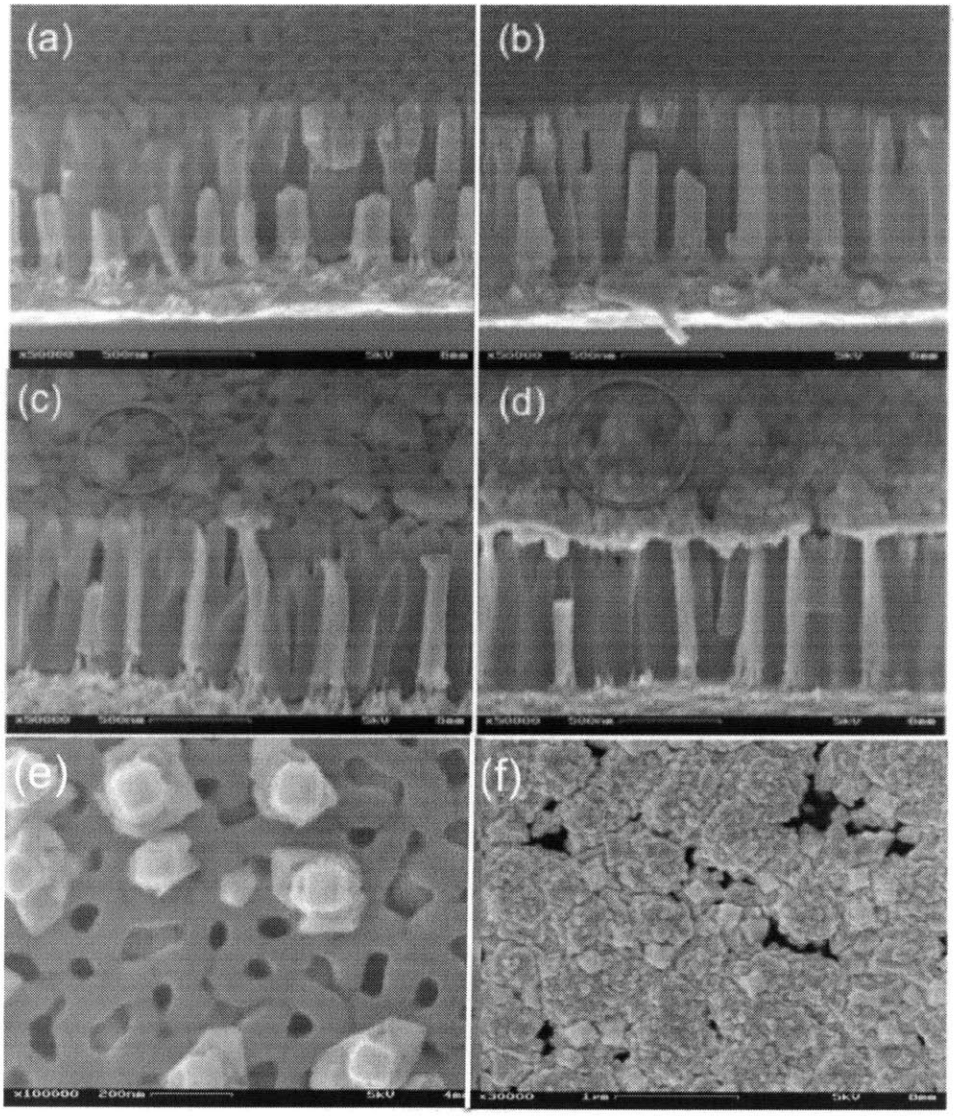

Figure 3.6 SEM images of the Au nanowire arrays with respect to the electrodeposition time. The elapsed times for (a), (b), (c), and (d) were 70s, 90s, 110s, and 180s, respectively. (e) and (f) are plan-view images of the sample (c) and (d), respectively. The vertically growing nanowires ((a) and (b)) started to grow three-dimensionally after filling the pores, as shown in (c) and (d). It is remarkable that the overgrown Au caps showed facets, as shown in the red circles in (c) and (d). (e) and (f) more clearly show the faceted overgrown Au with 4-fold symmetry.

dimensionally after filling the pores. It is particularly remarkable that the overgrown Au 'cap's above the pores were faceted as shown in (c) and (d) (red circles). Fig. 3.6(e) and (f), the plan view images of the sample (c) and (d), respectively, more clearly showed faceted cap shapes with 4-fold symmetry. More detailed analysis regarding this behavior will be discussed in the following section.

To obtain freestanding Au nanowire arrays on the Au substrate, the AAO scaffolds and W layer were selectively etched using an etchant a 25 wt.% tetramethylammonium hydroxide (TMAH, SACHEM, INC) solution at 60°C for 2 hours. The resulting Au nanowire arrays with 80 nm diameters and 200 nm spacing are shown in Figure 3.7, for which (a) and (b) were obtained after the wet etching process of the samples in Fig. 3.6(b) and (c), respectively. Clear facets of the Au caps can be observed in Fig. 3.7(b) inset.

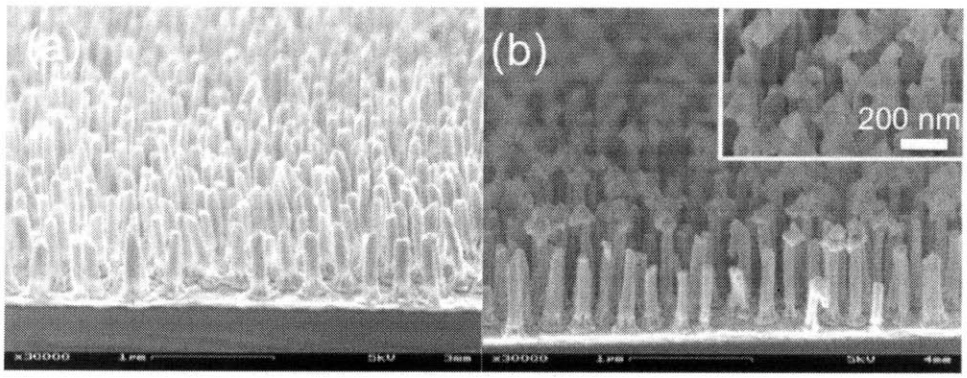

Figure 3.7 Freestanding Au nanowire arrays on the Au substrate. (a) and (b) are cross-sectional SEM images taken after an etching process to selectively remove the AAO scaffolds and W layer of the sample in Figure 3.6(b) and (c), respectively. The faceted caps are clearly observed in (b) inset. The process was conducted using a 25 wt.% tetramethylammonium hydroxide (TMAH, SACHEM, INC) solution at 60°C for 2 hours.

For microstructural analysis of the nanowires using TEM, the Au nanowire arrays with 15 nm diameters and 50 nm spacing were synthesized by electrodeposition in AAO scaffolds under hard anodization conditions as shown in Figure 3.4(b) and (d). The eletrodeposition condition was identical to what was applied for the AAO scaffolds prepared under the mild anodization; therefore, a similar cathodic voltage vs. time curve resulted. Figure 3.8(a) and (b) show SEM images of the Au nanowires with respect to the

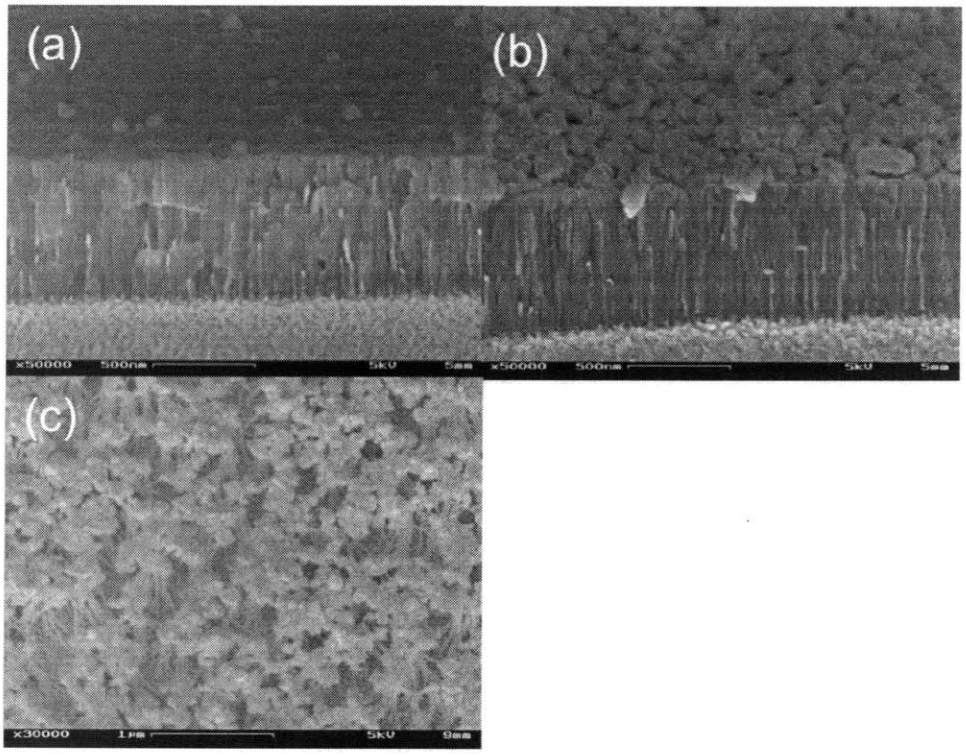

Figure 3.8 Cross-sectional SEM images of the Au nanowire arrays with respect to the electrodeposition time. Like the thick nanowires in Fig. 3.5, the Au nanowires grew three-dimensionally after filling the pores as shown in (a) and (b). Facets of the overgrown Au were found in this case as well. In the contrast with the thick nanowires in Fig. 3.7, these thin Au nanowires were clumped together after etching the AAO and W, due to their surface tension and high aspect ratio, as shown in (c).

electrodeposition time. Likewise for the thick Au nanowires in Fig. 3.5, the vertically growing nanowires in pores expanded three-dimensionally with facets after filling the pores. Freestanding Au nanowire arrays after etching the AAO scaffolds and W layers of the sample Fig. 3.8(b) are also shown in Fig. 3.8(c). On the contrary to Fig. 3.7, the Au nanowires were clumped together due to their surface tension and high aspect ratio.

The Au nanowires were also fabricated in the AAO scaffolds under mild anodization of the substrate B. It was desired that texture information for the only the Au nanowire arrays, because the Au nanowire arrays on substrate A (Fig. 3.7) showed crystallographic information for both the Au nanowires and the thin film layer used as a working electrode. A similar anodic current vs. time curve to Fig. 3.1 was obtained during the anodization process. After WO_3 etching, the Au nanowire array was fabricated through an electrodeposition process. Figure 3.9 shows cross-sectional SEM images of the Au naowire array on the Pt layer with respect the electrodeposition time. The same behavior observed in Fig. 3.5 appeared. The nanowires that were vertically growing in the pores ((a)-(b)) began to grow 3-dimensionally after completely filling the pores ((c)-(d)). The faceted overgrown caps also formed like the overgrown Au nanowires on the Au layer, but the morphology of the caps was somewhat different. As shown in Fig. 3.9(d) inset, the caps seem to have a dendrite-like shape, compared to the pristine surface shown in the Fig. 3.7(b) inset.

- Pt nanowires

  To compare with the Au nanowires, Pt nanowires were also synthesized. As stated

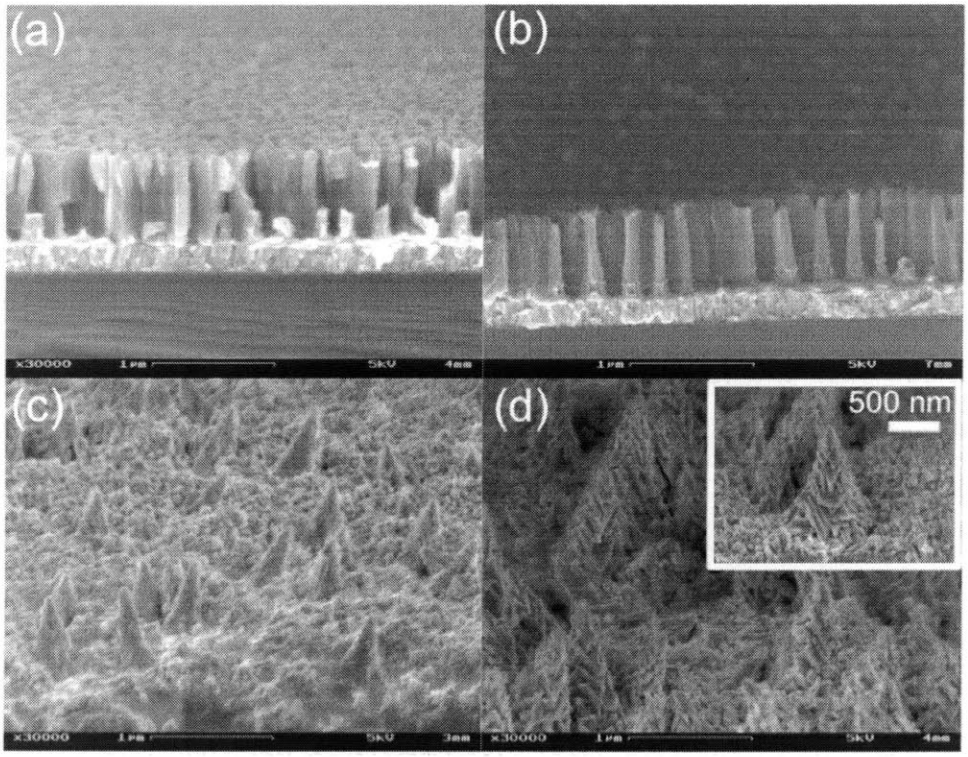

Figure 3.9 Cross-sectional SEM images of Au nanowire arrays on Pt substrates with respect to the electrodeposition progress. As seen in Fig. 3.5, the vertically growing nanowires in pores ((a) and (b)) started to grow out of the pores, forming faceted caps ((c) and (d)). Interestingly, the morphology of the caps seems to develop a dendrite-like shape, as clearly shown in the (d) inset.

in 2.2.3, the Pt was electrodeposited by applying the constant voltage 0.01 V with respect to a Ag/AgCl reference electrode. To determine an appropriate voltage for Pt electrodeposition, a linear current-voltage sweep from -0.5 V to 0.5 V with respect to the reference electrode was first implemented. As a result, a current-voltage curve with a negative current value below 0.1 V was obtained, indicating that the reduction of Pt occurred below 0.1 V. In addition, there was a peak at around -0.4 V, where H_2 reduction

happened. To have stable Pt reduction and avoid H_2 evolution, 0.01 V with respect to the reference electrode was chosen as the applied voltage for Pt electrodeposition. Figure 3.10 shows a current vs. time curve (blue curve) obtained from a Pt electrodeposition process in the AAO scaffolds fabricated through mild anodization on the substrate A. The charge transfer during the process is also shown on the figure (black cure), which indicates that only the Pt reduction process happened without a side reaction. With the same criteria applied in the Au electrodeposition process, the Pt electrodeposition process can be analyzed by dividing it into three steps after an activation step (0-85s); the nucleation of Pt (85-220s), vertical growth in pores (220-770s), and bulk growth out of pores (after 770s). During the growth of Pt in pores to form nanowires, the current, i.e.

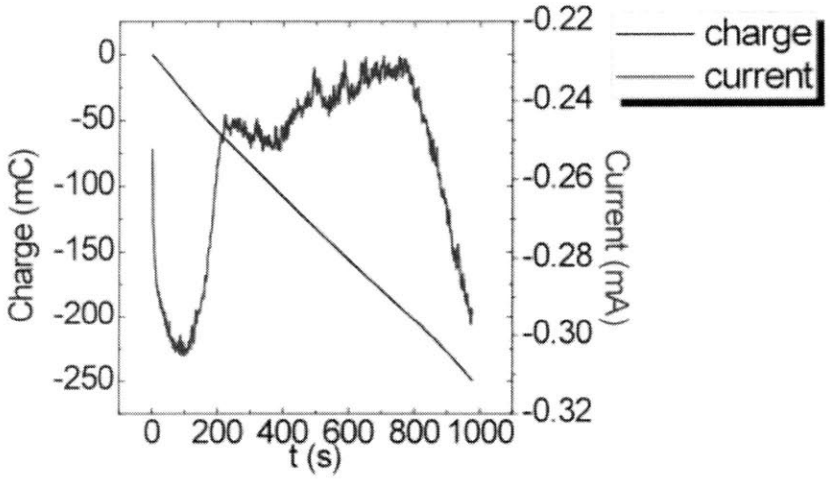

Figure 3.10 A current vs. time curve from a Pt electrodeposition process on substrate A. After an activation step (0-85s), the process occurred via three steps like the Au electrodeposition; nucleation (85-220s), growth in pores (220-770s), and three-dimensional growth out of pores (after 770s). By monitoring the curve, it was possible to decide when to stop the process to obtain a nanowire arrays without overgrowth.

the growth rate, gradually decreased. Note that the current value was negative. This was attributed to the increased resistance due to the confinement effect due to the AAO scaffolds that made the current decrease to maintain the given electric field across the electrodeposition solution. When the electrodeposition was completed in pores, the current started to increase, indicating that three-dimensional growth of Pt out of pores. Like the Au electrodeposition, the growth rate of Pt nanowires can be roughly deduced from the curve. It was 1.0 nm/s, which was much lower than the growth rate of Au nanowires.

Figure 3.11 shows SEM images of the Pt nanowire array grown on substrate A with respect to the deposition time. Corresponding electrodeposition times for (a)-(e) were 600s, 680s, 800s, 880s, and 1000s, respectively. (f)-(j) are corresponding cross-sectional SEM images to (a)-(e), respectively. To observe the evolution of nanowire length, the images were taken with the AAO scaffolds. Like the Au nanowires, the vertically growing Pt nanowires in pores ((a) and (f)) started to grow three-dimensionally out of pores after filling the pores ((b)-(e), (g)-(j))). Finally, the overgrown Pt formed boundaries with neighboring overgrown Pt when the width extended to about 200 nm. It should be noted that in contrast with Au, the overgrown Pt caps were not faceted, but swelled up.

A freestanding Pt nanowire array was obtained through the same wet etching process as the Au nanowires by selectively removing the AAO scaffolds and W. Figures 3.12(a) and (b) show cross-sectional SEM images taken after etching the samples shown in Fig. 3.11(f) and (g), respectively. Like the Au nanowires, the Pt nanowires were not been modified during the etching process.

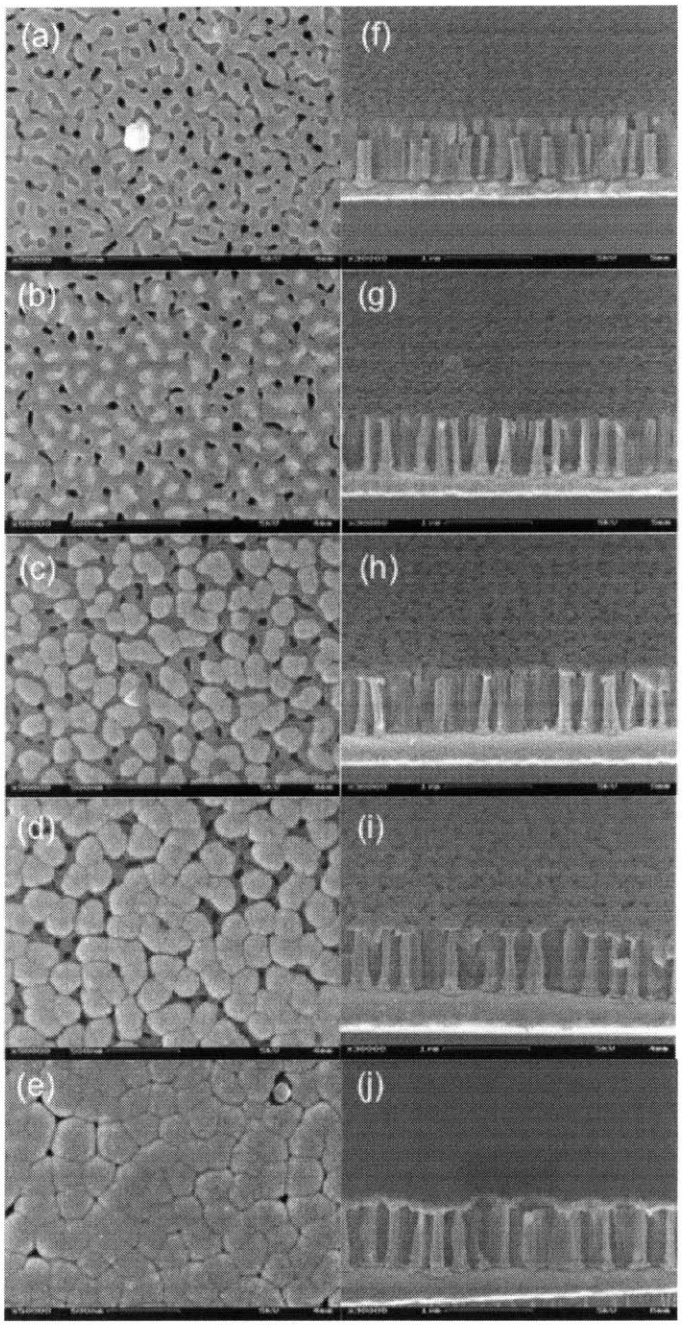

Figure 3.11 SEM images of the Pt nanowire array with respect to the electrodeposition time. (a)-(e) are plan-view SEM images with elapsed deposition times of 600s, 680s, 800s, 880s, and 1000s, respectively. (f)-(j) are corresponding cross-sectional SEM images to (a)-(e), respectively. In contrast with the Au nanowires, there were no clear facets in the overgrown Pt caps.

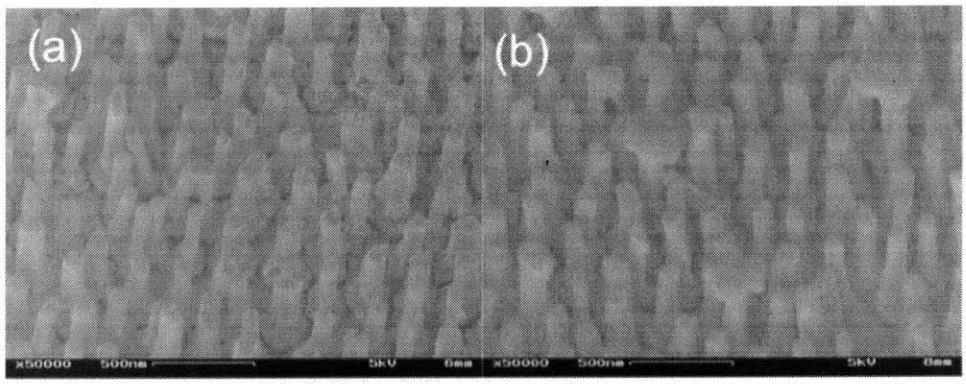

Figure 3.12 Cross-sectional SEM images of the freestanding Pt nanowire array. (a) and (b) were obtained after etching the AAO scaffolds and W of the samples in Fig. 3.11(f) and (g), respectively, with the same conditions applied for the Au nanowires.

Like the Au nanowires, for the TEM analysis of the Pt nanowire array with 15 nm pore diameters and 50 nm spacing obtained by electrodeposition in the AAO scaffolds prepared under the hard anodization conditions as shown in Fig. 3.4(b) and (d). The eletrodeposition condition was identical to the Pt nanowire growth in the AAO scaffolds prepared under the mild anodization conditions. Therefore, a similar cathodic voltage vs. time curve was obtained. Figure 3.13 shows SEM images of the resulting thin Pt nanowires with respect to the electrodeposition time. The images were taken after etching the AAO scaffolds and W. Like the Au nanowires as shown in Fig. 3.8(c), the Pt nanowires were clumped together because of their surface tension and high aspect ratio. However, facets were not observed in the overgrown Pt caps.

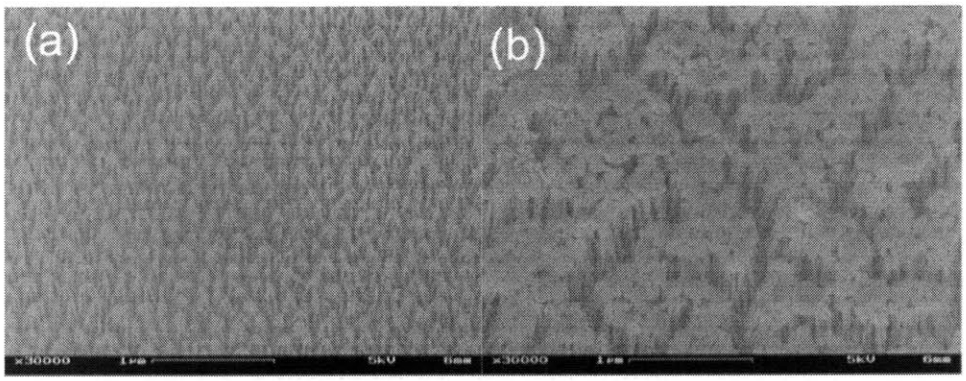

Figure 3.13 Cross-sectional SEM images of Pt nanowire arrays with respect to the electrodeposition time. The images were taken after etching the AAO scaffolds and W. Like the thick nanowires in Fig. 3.11, the Pt nanowires grew three-dimensionally after filling the pores. The Pt nanowires were clumped together like the Au nanowires in Fig. 3.8(c), but facets were not observed in the overgrown Pt caps.

3.3 Texture and Microstructure analysis

3.3.1 X-ray Diffraction (XRD)

- Au nanowires

The collective crystallographic texture of the collective Au nanowires was analyzed using X-ray diffraction (XRD). The measurement was implemented with a typical theta-2theta mode from 30° to 90° of 2theta. Seven Au nanowire arrays with different lengths and different substrates were prepared. AuNW#1, AuNW#2 and AuNW#3 denote the freestanding Au nanowires grown in the AAO scaffolds prepared via the mild anodization of substrate A (Au substrate). AuNW#1 was grown in pores and AuNW#2 just completely filled the pores, and AuNW#3 was overgrown. In addition, the labels AuNW#4, AuNW#5, AuNW#6, and AuNW#7 indicate the Au nanowires grown in the AAO scaffolds prepared via the mild anodization of substrate B (Pt substrate).

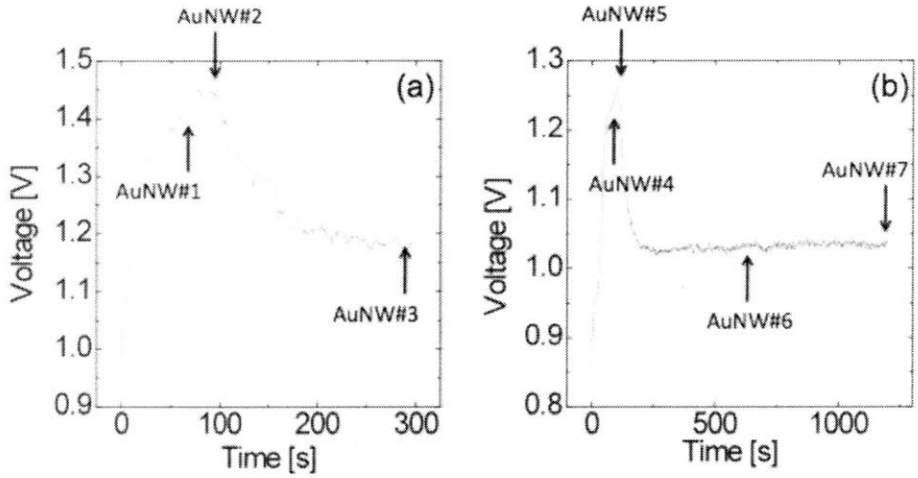

Figure 3.14 Voltages for growth of Au nanowires prepared for XRD analysis with respect to the electrodepsosition time. (a) corresponds to the Au nanowires fabricated on substrate A (Au substrate) whereas (b) was on substrate B (the Pt substrate).

AuNW#4 grew in pores and AuNW#5 just completely filled the pores, and AuNW#6 and AuNW#7 were overgrown. The electrodeposition time of each sample is shown in Figure 3.14.

As a reference, an Au thin film on the substrate D (Au substrate without the AAO scaffolds) made by electrodeposition was also prepared. The electrodeposition was conducted for 5 minutes, maintaining 1.0 mA/cm^2 with the same current density as the Au nanowire fabrication. The resulting thickness of the film was 500 nm, which was confirmed by a profilometer (Tencor, P16). As can be seen in Figure 3.15, both the Au substrate prepared by the electron beam evaporation (a) and the Au thin film (b) were poly-crystalline. However, the thin film was relatively much rougher than the substrate.

XRD results of the AuNW#1, AuNW#2 and AuNW#3 as well as the Au substrate and the thin film are illustrated in Figure 3.16. The Au peak positions were confirmed

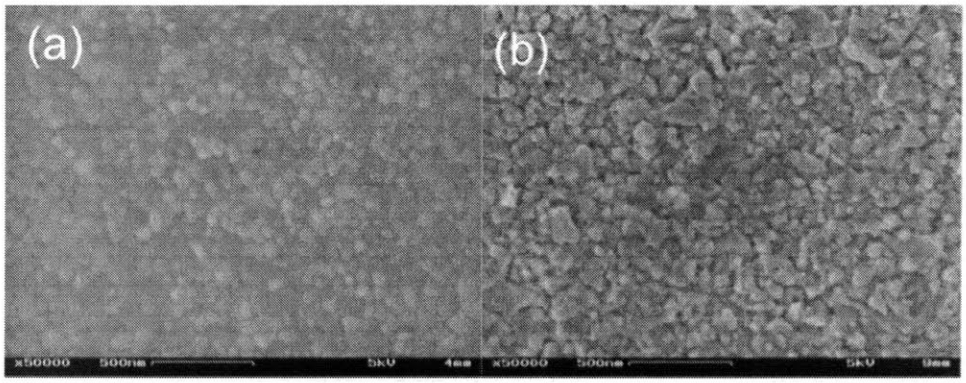

Figure 3.15 Plan-view SEM images of substrate D: (a) a Au/Ti stacked thin film on a wafer without AAO scaffolds (a), and (b) the 500 Au thin film made by electrodeposition. The surface of (b) was much rougher than (a).

using the Joint Committee on Powder Diffractoin (JCPDS) card with the reference code of 00-004-0784. The intensity on the y-axis has arbitrary units. Since a 1° offset was employed during the 2theta measurement, the strong peak intensity from the silicon substrate around 69° and 76° was avoided. The peak around 41° was verified to correspond to the Au_3Ti intermetallic phase. As can be seen in the figure, the Au substrate was very strongly textured in the [111] direction. On the other hand, the Au nanowire arrays growing in pores (AuNW#1 and AuNW#2) and the Au thin film showed other orientations such as [100] and [110], although the intensity of corresponding Au (200) and Au (220) peaks were low. This suggested that the Au nanowires grown in pores were poly-crystalline like the Au thin film deposited by electrodeposition. It was highly remarkable that the overgrown Au nanowires out of pores (AuNW#3) showed a strong intensity at the Au (200) peak position. This result can be correlated with the faceted overgrown Au, which was already described in the previous section. The facets were

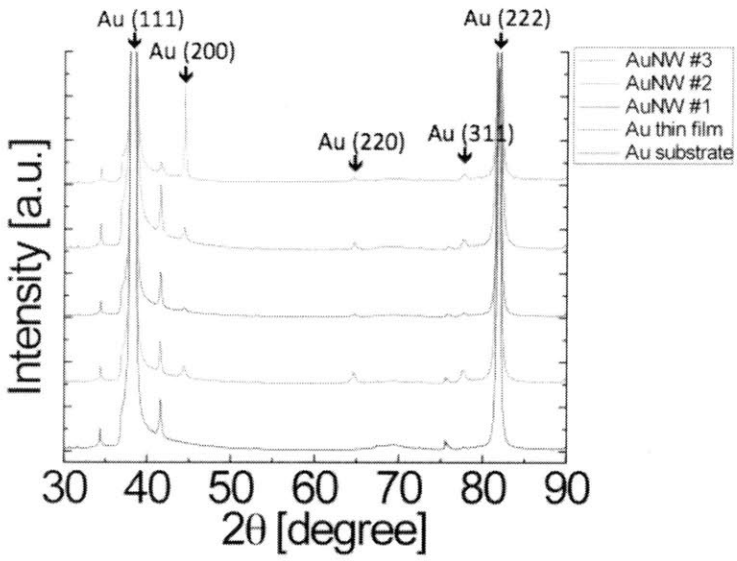

Figure 3.16 The XRD results for Au nanowires and Au thin film on a Au substrate. The Au substrate was strongly textured along [111] direction whereas the Au thin film and the Au nanowires grown in pores (AuNW#1 and AuNW#2) showed other growth textures, such as [100] and [110]. It was remarkable that the overgrown Au (AuNW#3) showed strong [100] texture, which can be attributed to the overgrown Au caps. The peak intensity without a significant change at the Au (111) and Au (220) peaks indicated that overgrowth of the Au occurred only along the [100] direction.

pyramidal in shape with 4-fold symmetry in the plan-view images. Therefore, it can be expected that the facets were (111) planes while the texture is along the [100] direction. On the contrary to the preferred texture along [100], the texture along other directions such as [111] and [110] was not perceived because there was not a significant change of the intensity of the corresponding diffraction peaks.

Although the strong [100] texture of the overgrown Au was confirmed from the XRD results in Fig. 3.16, the intensity from the Au (111) planes included the diffraction from the highly [111] textured Au substrate. To obtain the diffraction information of the

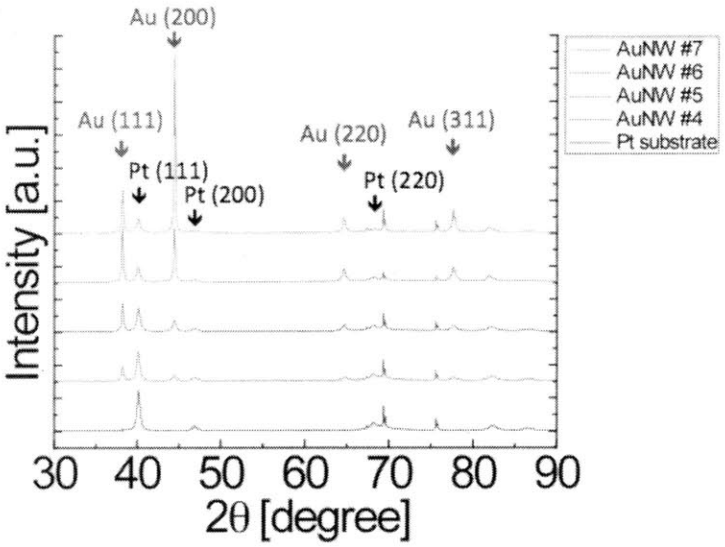

Figure 3.17 XRD results for Au nanowires grown on the Pt substrate. Non-textured Au nanowires grow in the pores (AuNW#4 and AuNW#5) and strongly [100] textured overgrown Au nanowires grow out of the pores (AuNW#6 and AuNW#7). The relatively narrow Au (200) peak width suggests that the overgrown Au out of pores might be single-crystalline or poly-crystalline with a large grain size.

only Au nanowires, the XRD of the Au nanowires grown on the Pt substrate was also carried out. Figure 3.17 shows the XRD results for AuNW#4, AuNW#5, AuNW#6, and AuNW#7. The intensity in the y-axis has an arbitrary unit. Like the Au diffraction pattern, the Pt pattern was also confirmed using a JCPDS card with the reference 00-004-0802. Although the Pt substrate was not highly textured like the Au substrate, the characteristics of the Au nanowire texture were similar to the Au nanowires on the Au substrate. As indicated in the figure, the Au nanowires grown in pores (AuNW#4 and AuNW#5) did not show an apparent texture whereas the overgrown Au nanowires were strongly [100] textured. Although the intensity of other peaks did not change significantly during the overgrowth, the intensity of the Au (200) peak was sharply increased. This can be also

owing to the faceted overgrown Au, implying this behavior was not dependant to the substrate used. Given the observation that the overgrown Au was highly [100] textured, the crystallinity of the overgrown Au caps could be presumed. Because the full width half maximum (FWHM) of the Au (200) in AuNW#7 was much narrower than for AuNW#4 and AuNW#5, the crystallite size of the overgrown Au was assumed to be large, as indicated using the Scherrer equation,

$$B(2\theta) = \frac{K\lambda}{L\cos\theta}, \tag{14}$$

with B(2Θ) being the peak width at the given 2theta, K the Scherrer constant, λ the wavelength of the X-ray, and L the crystallite size. In other words, the overgrown Au can be presumably single-crystalline or poly-crystalline with a large grain size.

- Pt nanowires

The collective crystallographic texture of Pt nanowire arrays was also analyzed via XRD, with the same measurement conditions as for the Au nanowires. Four Pt nanowire arrays with different lengths according to the electrodeposition time were prepared. PtNW#1, PtNW#2, PtNW#3 and PtNW#4 denote the Pt nanowires shown in Fig. 3.11(f), (g), (i) and (j), respectively. To compare with the Pt nanowire texture, a 500 nm Pt thin film was also prepared on substrate D (a Au substrate) with the same electrodeposition conditions employed to fabricate the Pt nanowires. The XRD results for the Pt nanowires and the Pt thin film are given in Figure 3.18. As can be seen in the figure, the most remarkable difference form the Au nanowires was that the Pt nanowires

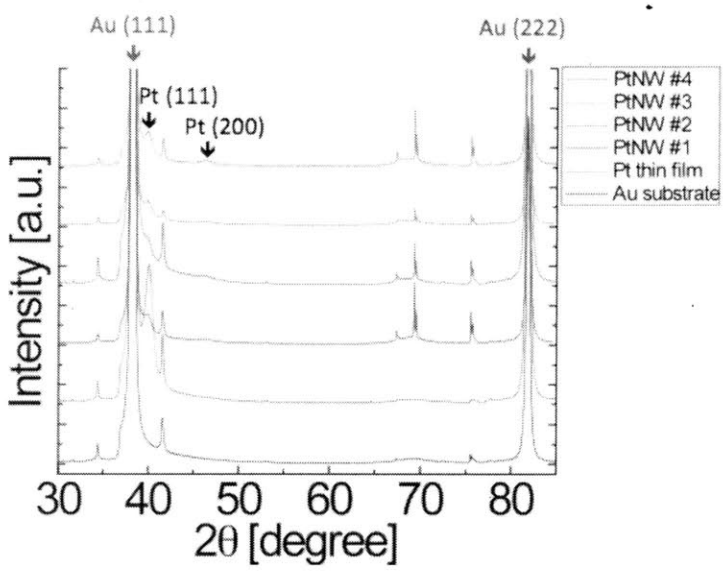

Figure 3.18 XRD results for the Pt nanowires and Pt thin film grown on a Au substrate. In contrast with the Au nanowires, the texture of the Pt nanowires was generally weak and there was not a notable texture change for growth in pores (PtNW#1 and PtNW#2) or overgrowth out of pores (PtNW#3 and PtNW#4). Moreover, the broad peak width for the Pt nanowires indicates that the crystallite size would is small.

were not textured, even after overgrowth. Although the Pt thin film showed a [111] texture, the peak intensities for all planes in the Pt nanowires were low and did not show a significant change with respect to the lengths. In other words, the overgrown Pt nanowires did not develop a texture change. This observation is in marked contrast with the overgrown Au. That the overgrown Pt was not faceted supports this result. In addition, relatively broader peak width for the Pt nanowires compared to the Au nanowires implies that the crystallite size of the Pt nanowires is smaller.

3.3.2 TEM analysis

The microstructure and crystallographic characteristics of individual nanowires

were studied via TEM. As stated in 2.3.3, the TEM samples were prepared by sonicating the freestanding nanowires. First, the overgrown Au nanowire array in Fig. 3.7(b) and an overgrown Pt nanowires array in Fig. 3.11(h) with 80 nm of diameter and 200 nm of spacing were prepared for the TEM. Figure 3.19 shows TEM images. As can be seen in this figure, a contrast between the faceted overgrown Au nanowire, (a), and the unfaceted overgrown Pt nanowire, (b), was clearly observed. However, size of each nanowire was not thin enough to transmit electrons, thereby making it hard to image microstructures such as grain boundaries. Therefore, a thin Au nanowire in Fig. 3.8(c) and a thin Pt nanowire in Fig. 3.12(b) with 15 nm diameter and 50 nm spacing were prepared for TEM analysis by sonicating the freestanding nanowire arrays.

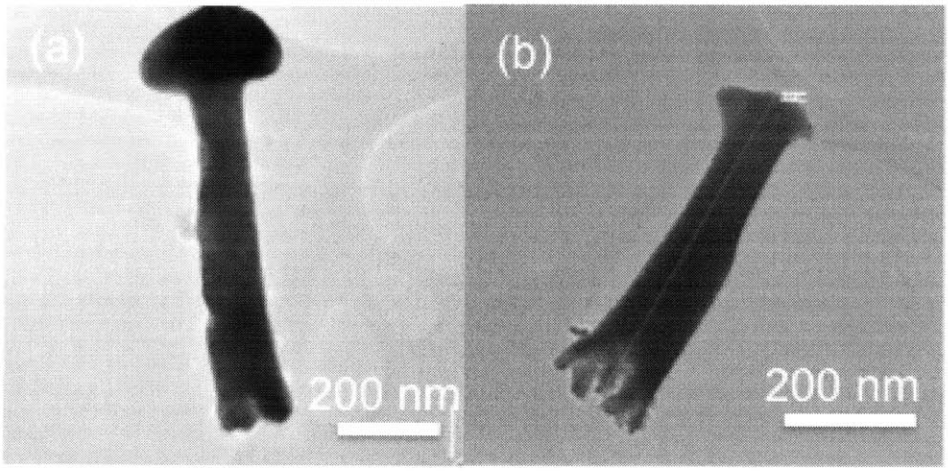

Figure 3.19 TEM images of an overgrown Au nanowire (a) and an overgrown Pt nanowire (b). Like the SEM results, while facets could be found in the overgrown Au nanowire, Pt did not show facets. However, due the relatively thick width of nanowires, microstructure information such as grain boundary locations was not easy to obtain.

- Au nanowires

Figure 3.20 shows TEM images of the thin Au nanowires. In contrast with the thick Au nanowire shown in Fig. 3.19(a), the nanowires were grouped together due to surface tension, as shown in Fig. 3.20(b). The microstructures of the Au nanowires

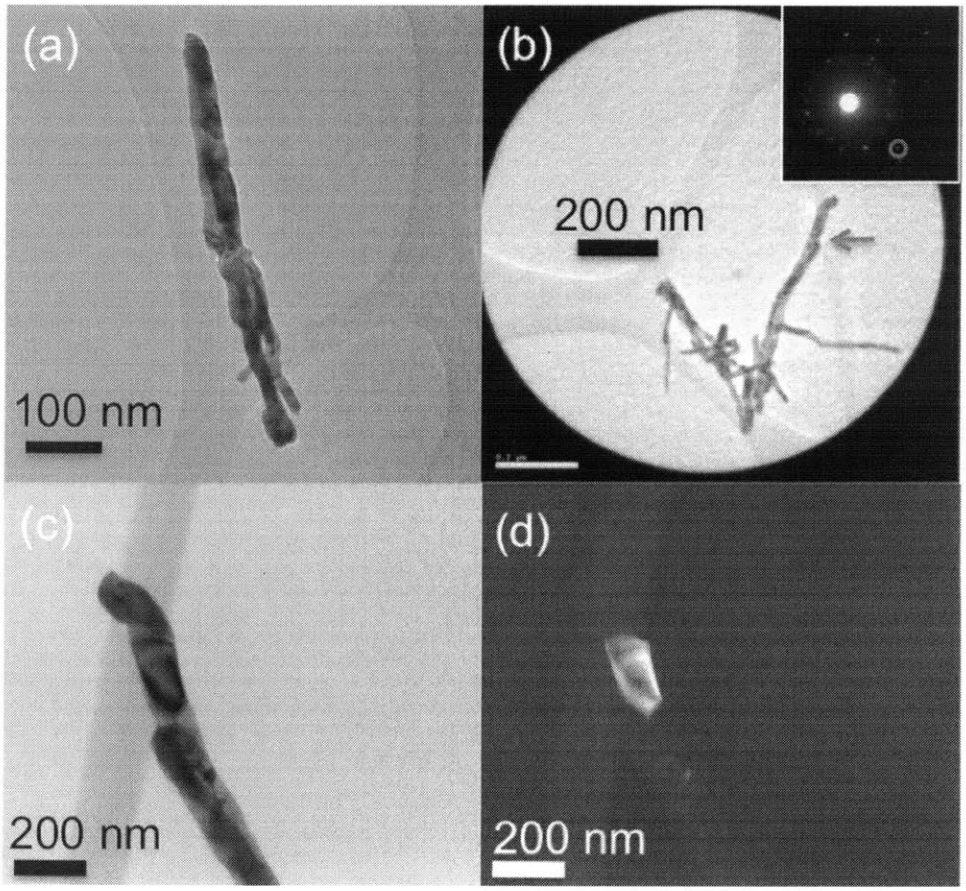

Figure 3.20 (a) TEM images of a thin Au nanowires. The microstructure of the nanowires appear to have bamboo-structures (a). (b) A SAED pattern of the collective Au nanowires indicates that they are poly-crystalline. By comparing a bright field (c) and a dark field (d) TEM image of the single nanowire (red arrow in (b)), the grain size of the Au nanowire could be deduced to about 200 nm. The corresponding plane was a {220} plane (red circle in the SAED pattern).

looked like bamboo-structures, as shown in (a). We also obtained a selected area electron diffraction (SAED) pattern (inset in (b)) for the collective Au nanowire array, (b), which indicated that the Au nanowires were poly-crystalline as confirmed via the XRD. In addition, the grain size of the nanowires was also measured by comparing a bright field (c) and a dark field (d) TEM images of a single nanowire (a red arrow in (b)) along [110] direction (a red circle in the SAED pattern inset in (b)). As a result, a grain size of about 200 nm was verified. Other grains were also expected to have similar sizes. In other words, the Au nanowires had poly-crystalline bamboo-structures with about 200 nm grain sizes, consistent with results reported elsewhere [48].

The faceted overgrown thin Au nanowire was also analyzed via the TEM. Figure 3.21 shows a TEM image with overgrown Au caps and corresponding SAED pattern (inset) of a cap (red arrow). In contrast with the ring-type pattern in the nanowire bundle shown in Fig. 3.20, the periodic spot array indicated that the Au cap was single crystalline. From possible single crystal SAED patterns that the face-centered cubic (FCC) structure can have [49], it was confirmed that the SAED pattern shown was based on a zone axis along the [110] direction. As a result, by comparing the pattern with the TEM image, it was also verified that not only did facets form normal to the [111] direction, but also the Au nanowire was growing along the [100] direction. These observations are in agreement with the expectation from the SEM and XRD results of the overgrown Au nanowires previously discussed. The plan-viewed SEM image showed facets with 4-fold symmetry and the XRD results showed a strong and narrow peak at the (200) position.

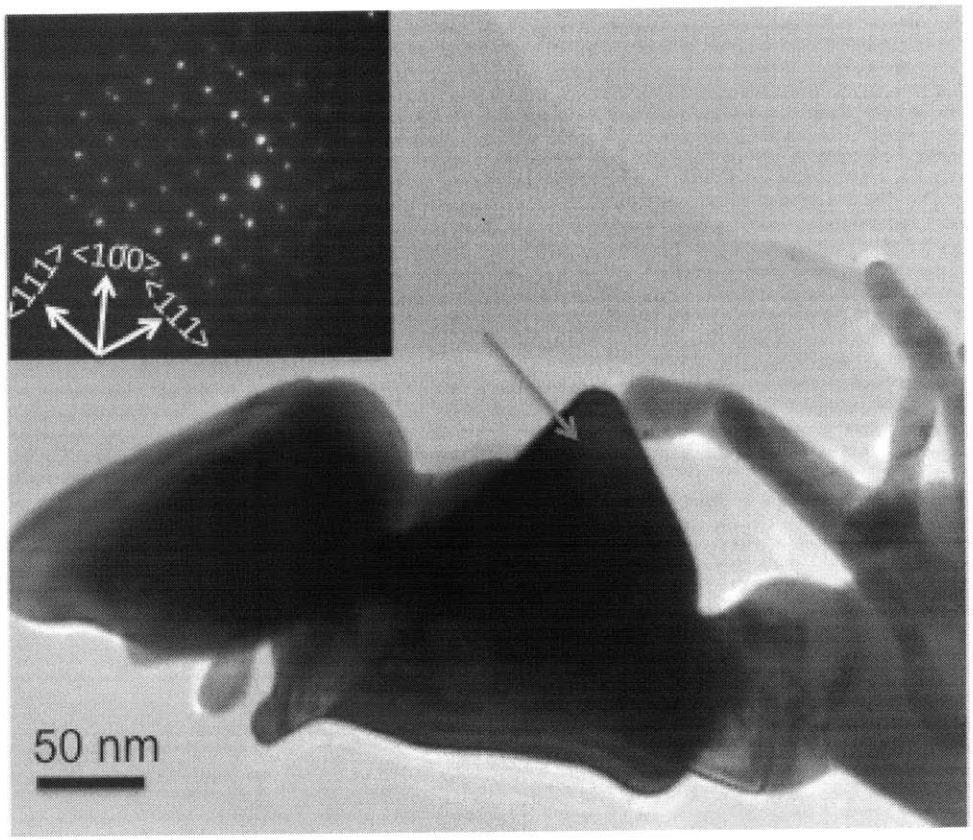

Figure 3.21 A TEM image with overgrown Au caps and an SAED pattern (inset) of a cap (red arrow). The SAED pattern indicates that the Au cap is single crystalline. Moreover, it can also be deduced that the facets are normal to the [111] directions and the growth direction was [100], which is in agreement with the interpretations from the SEM and XRD results.

- Pt nanowires

Figure 3.22 shows TEM images of a thin Pt nanowire. The microstructure shown in the highly magnified image (b) was clearly different from that of the Au nanowire. The Pt nanowire appeared to be poly-crystalline, like the Au nanowire, from a SAED pattern obtained (not shown). However, as can be seen in the TEM images, grains were not clearly defined, but very tiny. This observation supports the SEM and XRD results;

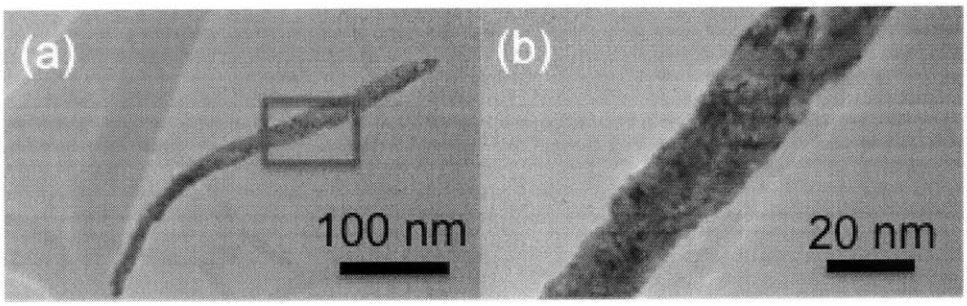

Figure 3.22 TEM images of a thin Pt nanowire. (b) is the highly magnified image of the nanowire shown in (a) (red rectangle). The microstructure of the Pt nanowire is clearly different from that of the Au nanowire. It seems to be poly-crystalline, but the grains were not clearly defined and very tiny.

overgrown Pt nanowires were not faceted and the diffraction peaks of the Pt nanowires were not only weaker, but also broader than those of the Au nanowires.

3.4 Summary

Au and Pt nanowires were fabricated in the AAO scaffolds using electrodeposition and then their texture and microstructure were analyzed using XRD and TEM. Interestingly, when the Au nanowires grew out of pores, the overgrown caps were faceted and were single crystals. On the other hand, the Pt nanowires were neither faceted nor single crystalline. In the following section, the origin of this behavior will be discussed.

Chapter 4. Discussion

4.1 The faceted overgrown Au nanowires

For the overgrown Au nanowire arrays, three remarkable behaviors were observed. First, the nanowires grown in pores were poly-crystalline without a specific texture. Second, the overgrown nanowires show a texture evolution to the [100] direction. Finally, the TEM result confirmed that the overgrown caps of the nanowires were single crystals with (111) facets and oriented with a [100] growth direction.

During the electrodeposition process for synthesis of nanowires, instead of the application of a constant voltage, a constant current density was maintained to achieve a constant growth rate. As a result, the cathodic voltage directly associated with the overpotential was varied with respect to the reaction time, as shown in Fig. 3.5 and Fig. 3.14. Since the ovepotential is one of the parameters defining the critical nucleus size (Eq. 11 and Eq. 13), a microstructure that depends on the change of the overpotential is obtained. As noted in 1.2.2, Au is known to be one of the metals for which 2D-like nucleation occurs in electrodeposition, and is consequently expected to easily form a single crystal structure [38]. Besides, the texture of the Au can be either [111] or [110], determined by the degree to which kinetics governs growth. It has been reported that the energetically favored texture dominates along the [111] under lower overpotential whereas higher overpotential kinetically favors the development of [110] texture. At intermediate overpotential, the formation of poly-crystalline structures due to the competition between two directions is expected [46-47]. With these arguments, it can be

understood that the poly-crystalline Au nanowires grown in pores result from an intermediate overpotential that is not enough to drive development of a texture along specific direction. Regarding the single crystalline Au caps, it has to be noted that cathodic voltage sharply dropped after having a maximum when the Au started to grow out of the pores. This indicates that the overpotential also followed the same trend. Taking a confinement effect by pore walls into account, the highest overpotential was obtained at the moment when the Au completely filled the pores. Since the texture changed to [100] after the overgrowth of Au, it seems likely that there was a new nucleation event occurred at this moment. Then, the dynamically and sharply lowered overpotential gave rise to an increase of the critical nucleus size for new nuclei, preventing a further nucleation event. In other words, approaching the equilibrium state, it is more probable that a single crystal structure will form. The (111) faceted caps can be attributed to the fact that the (111) plane has the lowest surface energy, as indicated in Table 4.1 [50]. It should be noted that this faceting behavior in overgrown Au nanowires is reported here for the first time. Overgrown nanowires in AAO usually have not been studied because the overgrown parts of the wires are not generally of interest [51], but also have not shown an interesting behavior [52].

For the texture evolution of the Au caps along the [100] direction, some theories are have been suggested to account for. First, surface stress induced by the confinement effect in the pores is taken into account. J. Diao et al. reported an atomistic simulation that <100> Au nanowires reorient to become <110> nanowires through the successive phase transformations from or the development of slip systems, both of which were driven by surface stress [53]. From what the authors claimed, a FCC <100> nanowire can

	Cu	Ag	Au	Ni	Pd	Pt
(111)	1170	620	790	1450	1220	1440
(100)	1280	705	918	1580	1370	1650
(110)	1400	770	980	1730	1490	1750
Experimental (average face)	1790	1240	1500	2380	2000	2490

Table 4.1 Calculated surface energies of the low-index planes and the experimental surface energy [50]

reorient into a base-centered-cubic (BCT) phase by tensile stress components in the length direction on the side surfaces of the nanowire. The BCT phase that is unstable with respect to shear deformation transforms to a FCC <110>. With a different simulation method, the authors showed a FCC <100> gold nanowire yielded by a surface stress reoriented to a FCC <110> through one {111}<112> slip system. This may explain the texture of the Au caps along [100], because this behavior can be interpreted as a restoring process for the initial [100] texture caused by relaxation of a surface stress applied during growth in pores. However, since this theory is based on a transformation process in a single crystal, it may be not reasonable to apply to the Au caps formed after a new nucleation step. Otherwise, the [100] texture can be discussed by interpreting the faceted Au caps as a kind of dendrite structure [54-56]. Cu and Au can form a dendrite structure using a surfactant-free electrodeposition by changing parameters such as the bias potential, electrolyte concentration, and temperature. In some cases, hierachical dendritic structures observed in Cu and Au show a similar shape to the Au caps. However, the faceted Au caps here cannot be regarded as a dendritic structure for the following reasons. First, generally dendritic growth requires relatively high overportential and high

deposition currents, i.e. growth rate. In the case of Au cap growth, not only did the current stay constant, but also the overpotential decreased. Second, in this experiment, a commercial electrolyte that might include additives to inhibit a dendritic growth was used for Au electrodeposition, Finally, even if a dendritic growth resulted in a complicated morphology, the change of a crystallographic texture was not reported. Hence, the texture-defining mechanism for newly nucleated Au caps is left open for discussion.

4.2 Different Behavior between the Au and Pt Nanowires

The Pt nanowires showed two characteristics different from the Au nanowiers. First, although the Pt nanowires were also poly-crystalline like as the Au nanowires, the grain size was much smaller, compared to the Au nanowires. Second, the overgrown Pt nanowires did show neither faceted caps nor the evolution of texture. It should be noted that the Pt nanowires were grown with a constant voltage application, in contrast to the Au nanowires that a constant current density was maintained. Namely, a constant overpotential was applied during the synthesis of the Pt nanowires. Therefore, if a new nucleation event occurred when the Pt grew out of the pores, a change of the critical nucleus size is not expected, and accordingly, the change of microstructure did not result. It is notable that the overgrown Pt did not show a texture evolution, in contrast with Au. It appears that the new nucleation was suppressed because the growth rate, or current, began to increase when the Pt grew out of the pores. The much smaller grain size than the Au nanowires are attributed to the inherent properties of Pt. As noted in 1.2.2, since the electrodeposition of Pt preferentially follows the 3D-like nucleation-coalescence growth, the Pt nanowires were expected to have a poly-crystalline structure. Moreover, it

appears that relatively high surface energy inhibited the surface diffusion of the deposited Pt atoms, thereby making it hard to have a large grain size [50].

Chapter 5. Summary and Future Work

5.1 Summary

Electrodeposition on porous alumina scaffolds is a convenient way to synthesize a functional nanowires array. One of the prerequisites to use the porous alumina as a scaffold was to selectively remove barrier-oxide in the pore base. With the matured technique to perforate pore base using a W interlayer, Au and Pt nanowires array were fabricated expecting functional applications. It was by accident that the faceted overgrown Au nanowires were observed while Pt did not show the characteristics. However, understanding of this interesting phenomenon was difficult because it turns out the process was very complicated, involving dynamic change of the overpotential during electrodeposition induced by a nanoconfinement. It is known that the growth mechanism of Au by electrodepsosition follows the 2D-like nucleation that is facile to form a single crystal structure. For the Au nanowire fabrication, a constant current density was maintained during the reaction and thus the cathodic voltage was resulted. When the Au began to grow out of pores, the voltage was sharply dropped and then saturated. Because the cathodic voltage was directly associated with the overpotential, which defines the critical nucleus size, the dynamic change of the voltage implied the evolution of the microstructure of the overgrown Au nanowires after a new nucleation event when the Au grew out of pores. The TEM and XRD results confirmed that the overgrown 'cap's were (111) faceted single crystal structure with [100] texture. The formation of the single crystal structure was attributed to the lowered overportential, making the critical nucleus

size increase during a new nucleation event and thus preventing the formation of grains. Regarding the mechanism through which Au caps developed a [100] texture, two possibilities were discusses, surface-stress-induced texture evolution and a kind of dendritic growth, but conclusive identification of a mechanism was not obtained. On the contrary, the Pt nanowires did not show the characteristics of Au nanowires. The Pt grown by electrodeposition generally follows the 3D-like nucleation that usually forms a poly-crystalline structure. It was also assumed that relatively high surface energy prevented the surface diffusion of the deposited Pt atoms, resulting in the small grain size.

5.2 Future Work

From the experimental results obtained, it is expected that the confinement effect by pore walls affects the overgrown Au nanowires somehow. Therefore, observation of the change of texture and microstructure with respect to pore diameter would be a good starting point for future study. It has been reported that the varied pore size drives the texture evolution of the nanowires [42, 57]. With fixed elctrodeposition condition, when pore diameter decreases, [110] texture becomes stronger. Conversely, the wider pore diameter, the more prominent [111] texture is observed. This was interpreted interpreted to suggest that the texture was defined by whether interface energy minimization of the nanowires with the pore walls or with the substrate dominated. When the pore diameter was small enough, the texture was along the [110] direction because the minimization of interface energy between nanowires and pore walls should be satisfied at first [42]. Taking into account that the overgrown Au nanowires formed faceted caps with a [100]

texture, it is noteworthy that how the Au caps develop a facet and a texture with respect to the texture of Au nanowires in pores, depending on the pore diameters. Moreover, although the AAO scaffolds used in this thesis were not ordered, pores array with perfect long-range order, and with controlled symmetry and pore locations, with uncoupled pore diameter and pore spacing, can be obtained by anodizing lithographically defined template [58, 59]. Figure 5.1 shows preliminary results of the templated porous alumina scaffolds with monodomain pores array, varying pore diameter. To guide pore formation with 200 nm of pore spacing, and with 4-fold symmetry of pores array, interference lithography (IL) was applied by exposing twice rotated by 90°. A mild anodization was achieved on the pre-templated Al/W/Au tri-layer. Consequently, highly periodic pores array with 80 nm of pore diameter and 200 nm of pore spacing was obtained, as shown in Fig. 5.1(a). The pores could be uniformly widened with post treatment with 5 wt.% of phosphoric acid solution. As shown in Fig. 5.1(b)-(d), it was possible to prepare highly ordered pores array with different pore diameter by controlling the treatment time. During the pore widening, the symmetry of pores array and pore spacing were conserved.

As well as the pore diameters, the variation of other parameters involving in the electrodeposition such as the ambient temperature and the pH of the electrolyte can be also tested to help understand the texture and microstructure of the Au and Pt nanowires.

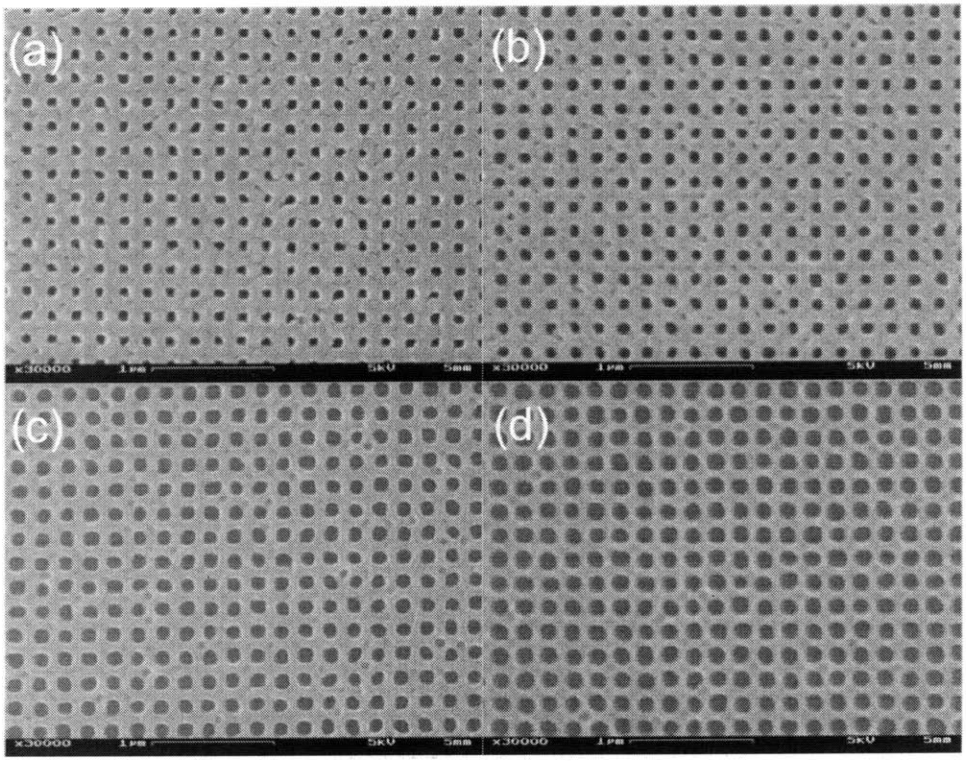

Figure 5.1 Monodomain porous alumina scaffolds prepared by interference lithography. First, the 4-fold symmetric pores array with 80 nm of pore diameter and 200 nm of pore spacing was fabricated shown in (a). By applying post treatment with 5 wt. % phosphoric acid solution, the pore were uniformly widened without the change of pore spacing or breaking of pore symmetry. With respect to the treatment time, the pores arrays with 110 nm, 135 nm and 155 nm of pore diameter were obtained shown in (b), (c) and (d), respectively.

References

[1] Diggle, J. W., T. C. Downie, and C. W. Goulding, "Anodic oxide films on aluminum," *Chemical Reviews* **69**(3), 365, 1969

[2] Young, L., *Anodic oxide films*, New York: Plenum Press, 1961

[3] *Anodic oxidation of aluminum and its alloys*, In Information Bulletin, vol. 14. London: The Aluminum development association, 1948.

[4] Keller, F., M. S. Hunter, and D. L. Robinson, "Structural Features of Oxide Coatings on Aluminum," *Journal of the Electrochemical Society* **100**(9), 411, 1953

[5] O'Sullivan, J. P. and G. C. Wood, "The Morphology and Mechanism of Formation of Porous Anodic Films on Aluminium," *Proceedings of the Royal Society of London Series A - Mathematical and Physical Sciences* **317**(1531), 511, 1970

[6] Thomposn, G. E., Y. Xu, P. Skeldon, K. Shimizu, S. H. Han, and G. C. Wood, "Anodic oxidation of aluminum," *Philosohpical Magazine B* **5**, 651, 1987

[7] Shimizu, K., K. Kobayashi, G. E. Thompson, and G. C. Wood, "A Novel Marker for the Determination of Transport Numbers during Anodic Barrier Oxide-Growth on Aluminum," *Philosophical Magazine B* **64**(3), 345, 1991

[8] Masuda, H. and K. Fukuda, "Ordered Metal Nanohole Arrays Made by a 2-Step Replication of Honeycomb Structures of Anodic Alumina," *Science* **268**(5216), 1466, 1995

[9] Martin, C.R., "NANOMATERIALS - A MEMBRANE-BASED SYNTHETIC APPROACH," *Science* **266**(5193), 1961, 1994.

[10] Xia, Y.N., Yang, Y. Sun, Y. Wu, B. Mayers, B. Gates, Y. Yin, F. Kim and H. Yan, "One-dimensional nanostructures: Synthesis, characterization, and applications," *Advanced Materials* **15**(5), 353, 2003

[11] Shingubara, S., "Fabrication of nanomaterials using porous alumina templates," *Journal of Nanoparticle Research* **5**, 17, 2003

[12] Zhan, Y., A. Kolmakov, Y. Lilach, and M. Moskovits, "Electronic contol of chemistry and catalysis at the surface of an individual Tin oxide nanowire," *Journal of Physical Chemistry B* **109**, 1923, 2005

[13] Lux, K. W. and K. J. Rodriguez, "Template synthesis of arrays of nano fuel cells," *Nano Letters* **6**, 288, 2005

[14] Wu, B., A. Heidelberg, and J. Boland, "Mechanical properties of ultrahigh-strength gold nanowires," *Nature Materials* **4**, 525, 2005

[15] Kline, T.R., M. Tian, J. Wang, A. Sen, M. W. H. Chan, and T. E. Mallouk, "Template-grown metal nanowires," *Inorganic Chemistry* **45**(19), 7555, 2006

[16] Yi, J. B., H. Pan, J. Y. Kin, J. Ding, Y. P. Feng, S. Thongmee, T. Liu, H. Gong, and L. Wang, "Ferromagnetism in ZnO Nanowires Derived from Electro-deposition on AAO Template and Subsequent Oxidation," *Advanced Materials* **20**, 1170, 2008

[17] Lee, W., H. Han, A. Lotnyk, M. A. Schubert, S. Senz, M. Alexe, D. Hesse, S. Baik, and U. Gosele, "Individually addressable epitaxial ferroelectric nanocapacitor arrays with near Tb inch^{-2} density," *Nature Nanotechnology* **3**, 402, 2008

[18] Oh, J., and C. V. Thompson, "Selective Barrier Perforation in Porous Aluminum Anodized on Substrates," *Advanced Materials* **20**, 1368, 203008

[19] Liu, L., E. Pippel, R. Scholz, and U. Gosele, "Nanoporous Pt-Co alloy nanowires: Fabrication, Characterization, and Electrocatalytic properties," *Nano Letters* **9(12)**, 4352, 2009

[20] http://www.crct.polymtl.ca/ephweb.php

[21] Despic, A.P., V. P., *Modern aspects of electrochemistry*, ed. J. O. M. W. Bockris, R. E.; Conway, B. E. Vol. **20**., New York: Plenum Press, 1989

[22] Lohrengel, M. M., "THIN ANODIC OXIDE LAYERS ON ALUMINUM AND OTHER VALVE METALS - HIGH-FIELD REGIME," *Materials Science & Engineering R-Reports*, **11**(6), 243, 1993

[23] Choi, J., "Fabrication of monodomain porous alumina using nanoimprint lithography and its appications," PhD Thesis, Mathematisch-Naturwissenschaftlich-Technische Fakultät, Martin-Luther-Universität Halle-Wittenberg, 2003

[24] Hoar, T.P. and N. F. Mott, "A mechanism for the formation of porous anodic oxide films on aluminium," *Journal of Physics and Chemistry of Solids* **9**(2), 97, 1959.

[25] Parkhutik, V. P. and V. I. Shershulsky, "Theoretical Modeling of Porous Oxide-Growth on Aluminum," *Journal of Physics D*, **25**(8), 1258, 1992

[26] Shimizu, K., R. S. Alwitt, and Y. Liu, "Cellular porous anodic alumina grown in neutral organic electrolyte II. Transmission electron microscopy examination of ultrathin cross sections and a model for film growth," *Journal of the Electrochemical Society* **147**(4), 1388, 2000

[27] Garcia-Vergarai, S. J., et al., "Mechanical instability and pore generation in anodic alumina," *Proceedings of the Royal Society a-Mathematical Physical and Engineering Sciences* **462**(2072), 2345, 2006

[28] Singh, G. K., A. A. Golovin, and I. S. Aranson, "Formation of self-organized nanoscale porous structures in anodic aluminum oxide," *Physical Review B* **73**(20), 205422, 2006.

[29] Houser, J. E. and K. R. Hebert, "The role of viscous flow of oxide in the growth of self-ordered porous anodic alumina films," *Nature Materials* **8**(5), 415, 2009

[30] Oh, J., "Porous Anodic Aluminum Oxide Scaffolds: Formation Mechanism and Applications," PhD Thesis, Department of Materials Science and Engineering, Massachusetts Institute of Technology, 2009

[31] Friedman, A. L., D. Brittain, and L. Menon, "Roles of pH and acid type in the anodic growth of porous alumina," *Journal of Chemical Physics*, **127**(15), 154717, 2007

[32] Li, A. P., et al., "Hexagonal pore arrays with a 50-420 nm interpore distance formed by self-organization in anodic alumina," *Journal of Applied Physics* **84**(11), 6023, 1998

[33] Masuda, H., F. Hasegwa, and S. Ono, "Self-ordering of cell arrangement of anodic porous alumina formed in sulfuric acid solution," *Journal of the Electrochemical Society* **144**(5), L127, 1997

[34] Jessensky, O., F. Müller, and U. Gösele, "Self-organized formation of hexagonal pore structures in anodic alumina," *Journal of the Electrochemical Society* **145**(11), 3735, 1998

[35] Masuda, H., K. Yada, and A. Osaka, "Self-ordering of cell configuration of anodic porous alumina with large-size pores in phosphoric acid solution," *Japanese Journal of Applied Physics Part 2-Letters* **37**(11A), L1340, 1998

[36] Lee, W., et al., "Fast fabrication of long-range ordered porous alumina membranes by hard anodization," *Nature Materials* **5**(9), 741, 2006

[37] Paunovic, M., M. Schlesinger, *Fundamentals of Electrochemical Deposition*, New York: Wiley, 1998

[38] Tian, M., J. Wang, J. Kurtz, T. E. Mallouk, and M. H. W. Chan, "Electrochemical Growth of Single-Crystal Metal Nanowires via a Two-Dimensional Nucleation and Growth Mechansim," *Nano Letters* **3**, 919, 2003

[39] Zhang, X. Y., L. D. Zhang, Y. Lei, L. X. Zhao and Y. Q. Mao, "Fabrication and characterization of highly ordered Au nanowire arrays," *Journal of Materials Chemistry* **11**, 1732, 2001

[40] Wang, J., M. Tian, T. E. Mallouk, and M. H. W. Chan, "Microtwinning in Template-Synthesized Single-Crystal Metal Nanowires," *Journal of Physical Chemistry B* **108**, 841, 2004

[41] Pan, H., B. Liu, J. Yi, C. Poh, S. Lim, J. Ding, Y. Feng, C. H. A. Huan, and J. Lin, "Growth of Single-Crystalline Ni and Co Nanowires via Electrochemical Deposition and Their Magnetic Properties," *Journal of Physical Chemistry B* **109**, 3094, 2005

[42] Wang, X. W., G. T. Fei, X. J. Xu, Z. Jin, and L. D. Zhang, "Size-Dependent Orientation Growth of Large-Area Ordered Ni Nanowires Arrays," *Journal of Physical Chemistry B* **109**, 24326, 2005

[43] Aslam, M., R. Bhobe, N. Alem, S. Donthu, and V. P. Dravid, "Controlled large-scale synthesis and magnetic properties of single-crystal cobalt nanorods," *Journal of Applied Physics* **98**, 074311, 2005

[44] Maurer, F., J. Brotz, S. Karim, M. E. T. Molares, C. Trautmann and H. Fuess, "Preferred growth orientation of metallic fcc nanowires under direct and alternating electrodeposition conditions," *Nanotechnology* **18**, 135709, 2007

[45] Wang, H. –J. et al., "Electrodeposition of tubular-rod structure gold nanowires using nanoporous anodic alumina oxide as template," *Electrochemistry Communications* **11**, 2019, 20094

[46] Switzer, J. A., H. M. Kothari, E. W. Bohannan, "Thermodynamic to kinetic transition in epitaxial electrodeposition," *Journal of Physical Chemistry B* **106**, 4027, 2002

[47] Budevski, E., G. Staikov, W. J. Lorenz, *Electrochemical Phase Formation and Growth: An introduction to the initial stage of metal deposition*, New York: VCH, 1996

[48] Peng, Y., T. Cullis, and B. Inkson, "Accurate electrical testing of individual gold nanowires by *in situ* scanning electron microscope nanomanipulators," *Applied Physics Letter* **93**, 183112, 2008

[49] Williams, D. B., C. B. Carter, *Transmission Electron Microscopy – Diffraction II*, New York: Plenum Press, 1996

[50] Foiles, S. M., M. I. Baskers, and M. S. Daw, "Embedded-atom-method functions for the FCC metals Cu, Ag, Au, Ni, Pd, Pt, and their alloys," *Physical Review B* **33**, 7983, 1986

[51] Yao, J., Z. Liu, Y. Liu, Y. Wang, C. Sun, G. Bartal, A. M. Stacy, and X. Zhang, "Optical negative refraction in bulk metamaterials of nanowires," *Science* **321**, 930, 2008

[52] Quach, D. V., R. Vidu, J. R. Groza, and P. Stroeve, "Electrochemical deposition of Co-Sb thin films and nanowires," *Industrial and Engineering Chemistry Research* **49**, 11385, 2010

[53] Diao, J., K. Gall, and M. L. Dunn, "Surface stress driven reorientation of gold nanowires," *Physical Review B* **70**, 075413, 2004

[54] Qiu, R., H. G. Cha, H. B. Noh, Y. B. Shim, X. L. Zhang, R. Qiao, D. Zhang, Y. I. Kim, U. Pal, and Y. S. Kang, "Preparation of dendritic Copper nanostructures and their characterization for electroreduction," *Journal of Physical Chemistry C* **113**, 15891, 2009

[55] Tao, F., Z. Wang, D. Chen, L. Yao, W. Cai, and X. Li, "Synthesis of silver dendritic hierachical structures and transformation into silver nanobelts through an ultrasonic process," *Nanotechnology* **18**, 295602, 2007

[56] Ye, W., J. Yan, Q. Ye, and F. Zhou, "Templated-free and direct electrochemical deposition of hierachical dendritic gold nanostructures: Growth and their multiple applications," *Journal of Physical Chemistry C* **114**, 15617, 2010

[57] Cortes, A., G. Riveros, J. L. Palma, J. C. Denardin, R. E. Marotti, E. A. Dalchiele, and H. Gomez, "Single-crystal growth of nickel nanowires: influence of deposition conditions on structural and magnetic properties," *Journal of Nanoscience and Nanotechnology* **9**, 1992, 2009

[58] Choi, J. S., G. Sauer, P. Goring, K. Nielsch, R. B. Wehrspohn, and U. Gosele, "Monodisperse metal nanowire arrays on Si by integration of template synthesis with silicon technology," *Journal of Materials Chemistry* **13**, 1100, 2003

[59] Krishnan, R and C. V. Thompson, "Monodomain high-aspect-ratio 2D and 3D ordered porous alumina structures with independently controlled pore spacing and diameter," *Advanced Materials* **19**, 988, 2007